REVIEW
SPACE PHYSICS: IONOSPHERE

Earth and Planetary Physics
4: 179–205, 2020
doi: 10.26464/epp2020028

Recent ionospheric investigations in China (2018–2019)

LiBo Liu[1,2,3,4*], and WeiXing Wan[1,2,3,4]

[1]Key Laboratory of Earth and Planetary Physics, Institute of Geology and Geophysics, Chinese Academy of Sciences, Beijing 100029, China;

[2]Innovation Academy for Earth Science, Chinese Academy of Sciences, Beijing 100029, China;

[3]Beijing National Observatory of Space Environment, Institute of Geology and Geophysics, Chinese Academy of Sciences, Beijing 100101, China;

[4]College of Earth and Planetary Sciences, University of the Chinese Academy of Sciences, Beijing 100019, China

Key Points:

- Ionospheric observations have continuously accumulated with increasing GNSS receivers being installed
- Studies of ionospheric climatology and space weather highlight new physical understanding
- Study of ionospheric irregularities/scintillations reports interesting features

Citation: Liu, L. B., and Wan, W. X. (2020). Recent ionospheric investigations in China (2018–2019). *Earth Planet. Phys.*, *4*(3), 179–205. http://doi.org/10.26464/epp2020028

Abstract: Since the release of the 2018 National Report of China on ionospheric research (Liu LB and Wan WX, 2018) to the Committee on Space Research (COSPAR), scientists from Mainland China have made many new fruitful investigations of various ionospheric-related issues. In this update report, we briefly introduce more than 130 recent reports (2018–2019). The current report covers the following topics: ionospheric space weather, ionospheric structures and climatology, ionospheric dynamics and couplings, ionospheric irregularity and scintillation, modeling and data assimilation, and radio wave propagation in the ionosphere and sounding techniques.

Keywords: ionosphere; ionospheric storm; ionospheric climatology; ionospheric irregularity; GNSS; space weather

1. Ionospheric Space Weather

Solar flare effects on the ionosphere have been investigated continuously. Previous studies revealed that solar flare effects on the ionosphere have a negative relationship with the solar zenith angle (SZA). The largest enhancement in electron density always occurs around the subsolar point. However, Le HJ et al. (2019) found that the enhancements in the total electron content (TEC) during six solar flare events in 2001–2014 were not strongly dependent on the SZA, with enhancement peaks rather far away from the subsolar point. The regions with the largest TEC enhancements seem to be in a zonal belt with a similar latitude. Spatial analysis of the TEC enhancements showed that such an anomaly distribution was not due to traveling ionospheric disturbances, and that the anomaly distribution was not related to the background neutral density. The anomaly distribution of TEC enhancements may therefore possibly be due to the combined effect of an enhancement in solar extreme ultraviolet (EUV) rays and transport processes induced by significant geomagnetic disturbances during the six solar flares.

Using ground-based and satellite measurements as well as model simulations, Zhao BQ et al. (2019) investigated the ionospheric response to the great 13–14 March 1989 magnetic storm. They found that the mid–low latitude ionosphere in East Asia was characterized during the main and recovery phases of the storm by strong westward electron density gradients persisting over a day at both the bottomside and topside of the ionosphere. Their study concludes that during superstorm events the ionospheric responses at nearby stations can be expected to be strongly different.

Liu LB et al. (2019) explored the responses of the ionosphere inside the disturbance composition zone to the October 2002 geomagnetic storms by using the long-duration continuous experiments of the Millstone Hill incoherent scatter radar (ISR). At Millstone Hill, the electron density often responds to geomagnetic disturbances considerably differently at lower altitudes than at higher altitudes. The prevalent change at low altitudes is a decrease in electron density; at topside altitudes, geomagnetic storms sometimes enhance or do not change electron densities significantly from quiet-time values. During geomagnetic disturbances, the values of h_mF_2 and the topside vertical scale height around 600 km become larger. Although the electron density exhibits different altitudinal responses, h_mF_2 and TEC still generally follow a similar pattern of depletions or enhancements. There are time-varying zonal differences in midlatitude TEC between Millstone Hill and a nearby location 28.5 degrees west (Figure 1). The zonal difference of TEC becomes stronger during storm times. The fine structure of ionospheric storm responses at middle and low latitudes (Zhao BQ et al. 2019; Liu LB et al. 2019) brings a great challenge to the capability of the models to predict space weather.

Correspondence to: L. B. Liu, liul@mail.iggcas.ac.cn
Received 30 SEP 2019; Accepted 13 NOV 2019.
Accepted article online 20 MAY 2020.

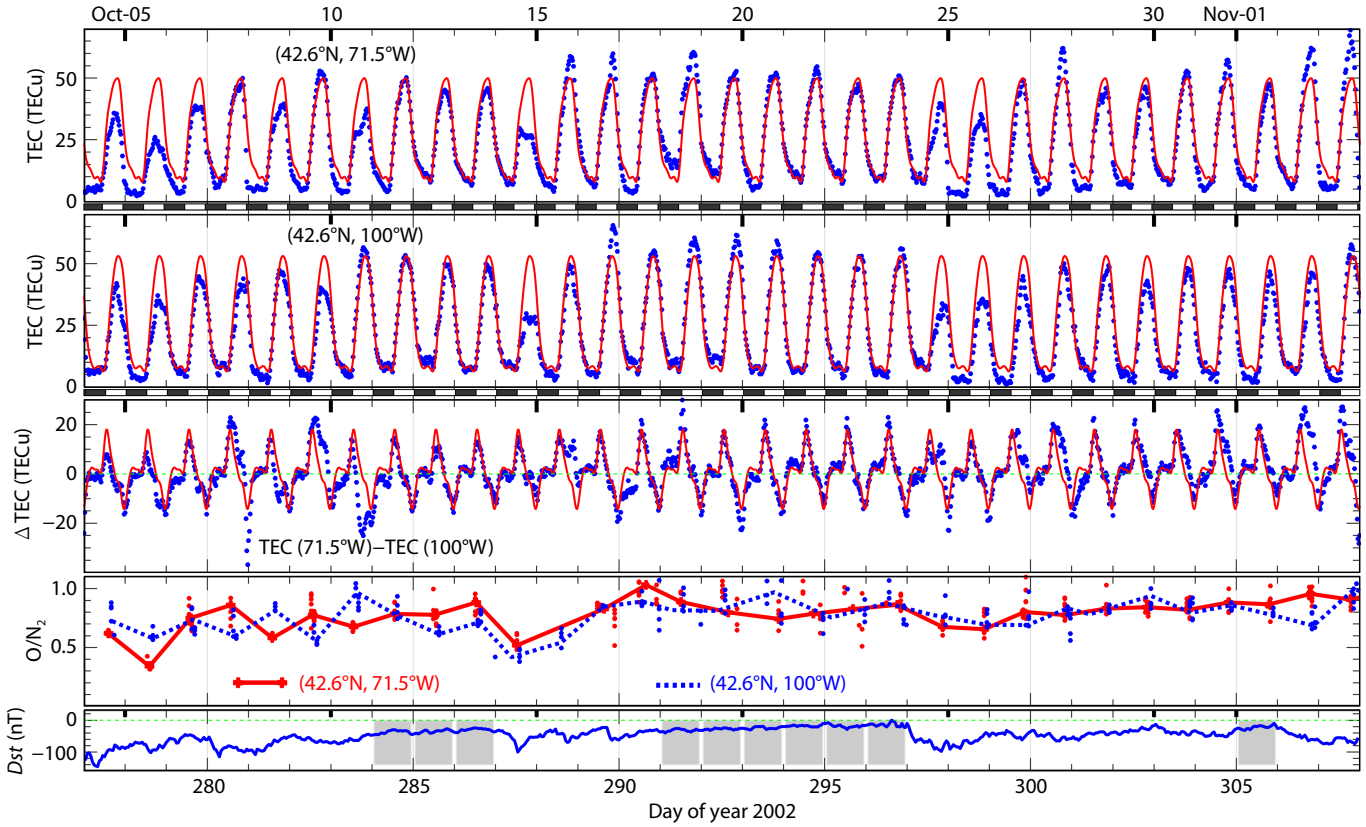

Figure 1. The top two panels plot total electron content (TEC) at Millstone Hill (42.6°N, 71.5°W) and at (42.6°N, 100°W). The blue points mark individual observations, and the red curve plots the daily medians of observations. The third panel displays differences of TEC between the two points. The fourth displays the O/N_2 ratio observations of TIMED/GUVI passing over Millstone Hill (42.6°N, 71.5°W) and a location to the west (42.6°N, 100°W), within a window of latitude ±2° × longitude ±2°. The bottom gives the *Dst* index. After Liu LB et al. (2019).

Zhang RL et al. (2019) investigated the response of the ionospheric electric field and currents to the solar flares and geomagnetic storm on 6–11 September 2017 using ISR and magnetometer observations over the Jicamarca sector. Significant differences are found in the response of ionospheric currents to the flare events. The increase and decrease of the ionospheric current are attributed to the enhanced conductivity in the initial stage of the solar flare and by the weakened electric field in the later stage, respectively. The disturbance of plasma drifts persisted for three days with westward polarities at ~10–16 LT and eastward at post-midnight and early morning. First, a downward disturbance plasma drift occurs at high altitudes around 10 LT; the disturbance amplitude increases with altitude from 200 to 500 km. The latitudinal structure of the disturbance winds is thought to be the possible source of the observed altitudinal variations in the disturbance plasma drift. The Jicamarca ISR observations show distinct altitudinal differences in the responses to the disturbance electric field of the F region electron density.

Zhang RL et al. (2018) investigated the disturbance field-aligned plasma drift in the equatorial topside ionosphere during eight selected geomagnetic storms from 2011–2015 using the Communication/Navigation Outage Forecasting System (C/NOFS) data. The disturbance field-aligned plasma drifts during the six solstice storms are found to flow from the winter to the summer hemisphere during morning–midnight hours but are indiscernible in the midnight–morning hours. During the two equinoctial storms any effects on the field-aligned plasma drift are minor. In terms of GPS–TEC and plasma temperature data from the Defense Meteorological Satellite Program (DMSP), the conjugate difference of storm-time disturbance plasma density gradient seems most likely to be caused by the disturbance winter-to-summer plasma drift, while the disturbance plasma temperature gradient shows a signature opposite to that of the disturbance plasma drift (Figure 2).

Jimoh et al. (2019) investigated topside ionospheric conditions during the September 2017 geomagnetic storm using up-looking TEC from GRACE, SWARM-A, TerraSAR-X, and MetOp-A satellites. Significant enhancements in TEC were present during the main phase of the storm, whereas no unusual enhancement was observed at the local morning and evening hours in the Asian-Australian sector during the recovery phase of the storm, as observed by Lei JH et al. (2018a). The ionospheric electric field disturbances were proposed to play an important role in triggering ionospheric irregularities under a relatively weak geomagnetic condition on 7 September 2017.

Balan et al. (2019) investigated ionosphere–thermosphere storms and low-latitude (630 nm) aurora by using several derived parameters (Ips*Dst*, Ips*Kp*, and Ips*AE*). The derived parameters representing the impulsive strength of geomagnetic storms seem to have more systematic dependence among themselves than among the intensities (Dst_{min}, Kp_{max}, and AE_{max}). The ionosphere–

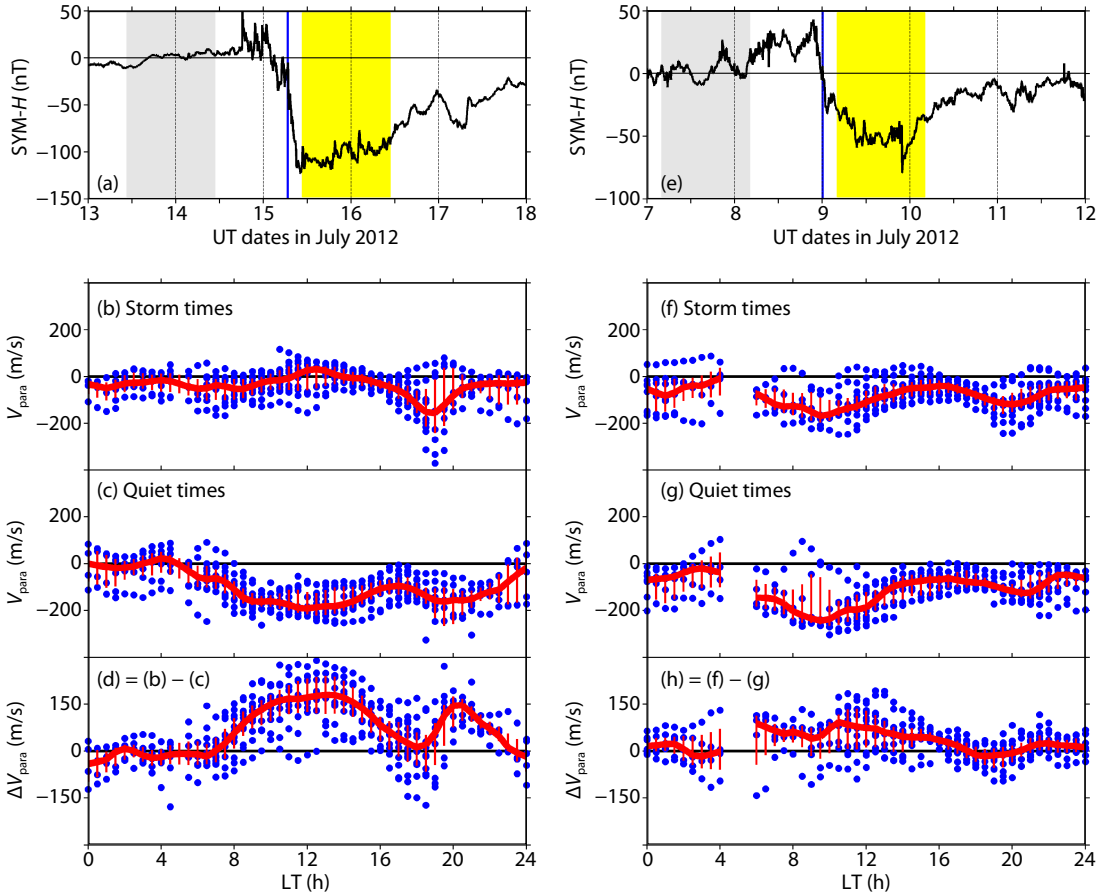

Figure 2. (a) The SYM-*H* index on 13–17 July 2012. The blue line marks the storm onset (at 06:42 UT on 15 July); yellow and gray areas indicate the 24-hour storm-time and 24-hour quiet-time intervals. (b) The blue dots denote the storm-time equatorial field-aligned plasma drifts observed by C/NOFS with red curve representing median and red lines denoting upper and lower quartile values. (c) Same as panel (b), but for the 24-hour quiet time interval. (d) The difference between (b) and (c). (e–h) Same as panels (a–d), but for the case on 7–11 July 2012 where the 24-hour quiet and storm intervals start at 04:12 UT on 7 and 9 July, respectively, after Zhang R et al. (2018).

thermosphere storms observed by the Challenging Minisatellite Payload (CHAMP) satellite and low-latitude auroras observed by optical imagers are much more intense during high impulsive storms than during high intensity storms. In a statistical sense, over 175 positive ionospheric storms ($\Delta h_mF_2>0$) observed in 1985–2005 and the intensity of 20 red auroras observed in 1989–2004 at midlatitudes correlate better with the impulsive parameters than the intensity parameters, with the best correlation being with Ips*Dst*. The mechanism of the impulsive action (high-energy input over a short duration) leading to large Ips*Dst* arises from the impact of fast solar storms (interplanetary coronal mass ejections) with large IMF B_z southward at their front (or shock). The impulsive action results in bright low-latitude auroras and strong ionosphere–thermosphere storms.

Zhang KD et al. (2019) investigated the ionospheric and thermospheric responses to oscillating interplanetary magnetic fields (IMF) B_z with 10-, 30-, and 60-min periods. The magnetosphere-ionosphere–thermosphere coupling system acts as a low-pass filter. There are two different thermospheric wind responses, almost simultaneous responses at different latitudes, and a typical traveling atmospheric disturbances signature with a time delay with respect to latitude.

Liu J et al. (2019a) comprehensively observed large-scale traveling ionospheric disturbances (LSTIDs) in the eastern Asian sector during the 2015 St. Patrick's Day (17 March 2015) geomagnetic storm (Figure 3). A LSTID spanning in longitude (80°E–140°E) occurred as a result of possible atmospheric gravity waves (AGWs) propagated equatorward, and the crest of this LSTID demonstrated a tendency to dissipate starting from the eastern side. The propagation parameters are of longitudinal dependence, probably related to the regional geomagnetic declination.

Li N et al. (2019) investigated the ionospheric response of the D region to solar flares. Their results show that a sharp decrease of the effective reflection height H' can be detected clearly from 76 km to 80 km during the non-flare period to nearly 58 km with flares, and a sudden increase of electron density (N_e) during 13 M-class flares. The changes of N_e are strongly correlated with the variation of X-ray flux, while the changes of H' exhibit a negative correlation with those of X-ray flux.

2. Ionospheric Structures and Climatology

Using ionospheric radio occultation data from the Constellation Observing System for Meteorology, Ionosphere, and Climate (COSMIC), Huang H et al. (2018) explored the longitudinal and alti-

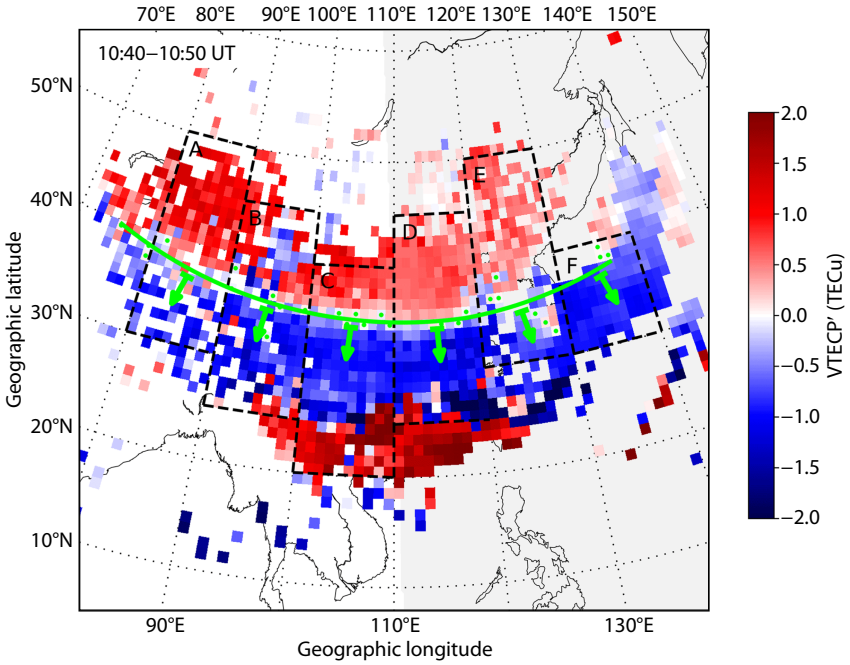

Figure 3. Map of TEC disturbances during 10:40–10:50 UT on March 17, 2015. After Liu J et al. (2019a).

tudinal patterns, during solstices, of the transition of interhemispheric asymmetry of equatorial ionization anomaly (EIA) (Figure 4). During the June solstice the stronger EIA peak transits from the winter to the summer hemisphere earlier in the sectors where the geomagnetic equator is farther away from the subsolar point and the geomagnetic field declination is larger; during the December solstice, the longitudinal variations generally show the opposite pattern. The upward/downward plasma movements in the summer/winter hemisphere are controlled by distance between the geomagnetic equator and subsolar point and the geomagnetic field configuration, leading to the different transition times in different longitudinal sectors. For both solstices, transition times emerge earlier as height increases, caused primarily by the larger effective scale height in the summer hemisphere than in the winter hemisphere, which results in a smaller electron density difference at higher altitudes with a fast transition.

Mo XH et al. (2018) studied the features of EIA crests by using the ionospheric TEC data observed from 2006 to 2015 at Nanning (22.84°N, 108.33°E). Both the value of TEC and the location of the northern EIA crest have a positive solar activity dependence and show a semi-annual variation, larger in equinoctial months than in

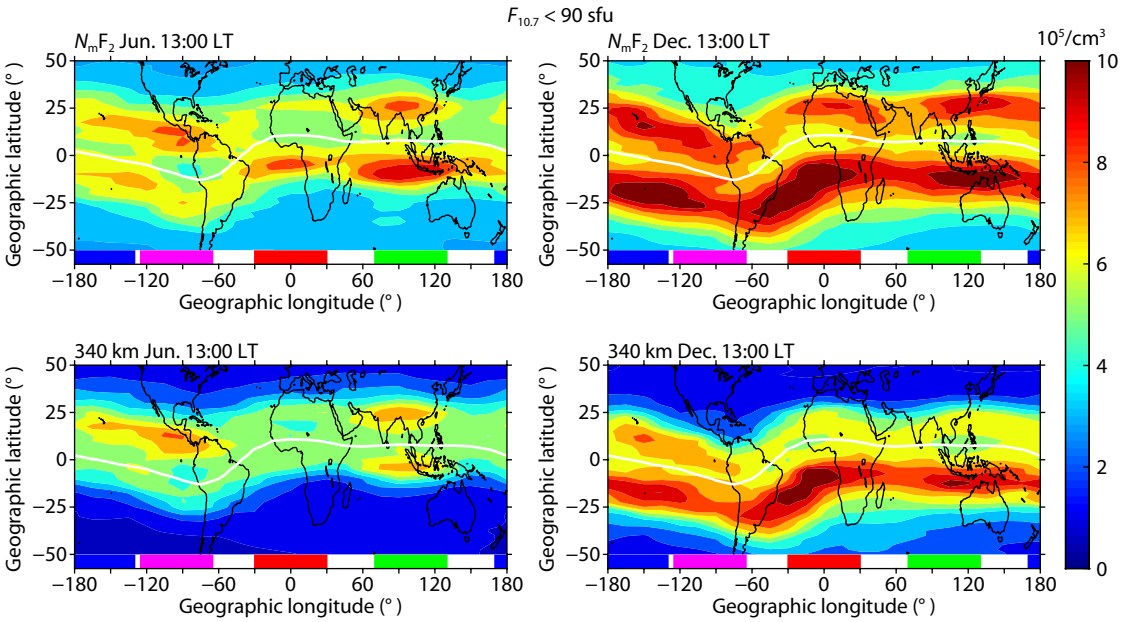

Figure 4. Electron density maps at h_mF_2 and 340 km at 13:00 LT during the June solstice (left) and December solstice (right) for $F_{10.7}$ < 90 sfu. The white line stands for the geomagnetic dip equator. After Huang H et al. (2018).

solstitial months. Their local time, seasonal, and solar cycle variations are consistent with variation in the strength of the equatorial electrojet (EEJ) (Figure 5). In particular, the EEJ strength has a stronger correlation with the EIA crest location than with the TEC value of the EIA crest.

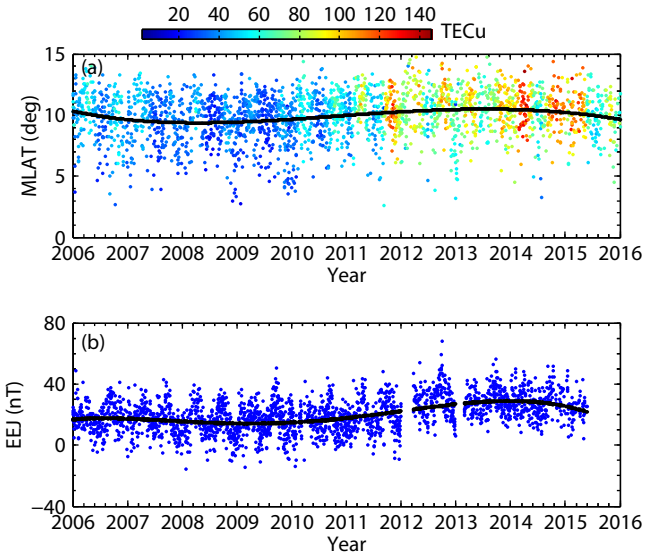

Figure 5. Day-to-day variations of the location of the northern EIA crest and the strength of EEJ from 2006 to 2015. After MO X et al. (2018).

Tian YY et al. (2019) studied the asymmetric EIA structure, especially a single peak in the latitudinal structure of electron density. The single crest phenomenon occurs frequently at longitudes where the double crest structure is weak. The longitudinal dependence is clearly observed at 10:00–18:00 local time, with zonal wave number 4 around equinox and 3 around winter solstice. This leads to the conclusion that the single crest phenomenon can be an indicator of the DE2 and DE3 components of nonmigrating tides, which modulate the wind field and thus the atmospheric dynamo electric field to cause the single or double crest structure.

Using 2006–2011 COSMIC electron density (N_e) profiles, Li QL et al. (2018) presented a comprehensive picture of the longitudinal variation of the mid-latitude (40°–50° mag. lat.) ionosphere at magnetically quiet times of low solar activity. The zonal difference of N_e is observed primarily above 220 km, caused by combined vertical drift effects driven by zonal and meridional winds. Zonal differences in the magnetic declination are the principal cause of the longitudinal difference in vertical drift driven by zonal winds, whereas the longitudinal difference in vertical drift driven by meridional winds is attributable primarily to zonal differences in the winds themselves.

Scale height is a key parameter to measure the electron density profile and ionospheric chemistry and dynamics. Longitudinal variation of scale height has not previously been investigated either in analyses or in empirical modeling. Li QL et al. (2019) retrieved the α-Chapman scale height from 11 years of lower topside ionospheric electron density profiles collected from COSMIC radio occultations. The midlatitude α-Chapman scale height shows evident longitudinal variations and its zonal structure shows a consistency with that of h_mF_2 during daytime. The authors present an empirical model that captures well the key temporal-spatial variations of the scale height.

Solar rotation (SR) variation dominates solar extremely ultraviolet (EUV) changes and significantly affects ionospheric variability on the timescale of days. The $F_{10.7}$ index is usually used as an indicator for solar EUV. $F_{10.7}$ was significantly enhanced during the 2008th–2009th Carrington rotations (CRs) owing to a very intense active region, causing the most prominent SR variation of $F_{10.7}$ during solar cycle 23 (Figure 6). Chen YD et al. (2018) found that the responses of $F_{10.7}$ and EUV to that intense active region were very discrepant. The $F_{10.7}$ response was much stronger than the EUV response so that the EUV–$F_{10.7}$ slope significantly decreased during the 2008th–2009th CRs, causing large errors when $F_{10.7}$ is used to estimate EUV and ionospheric electron density. The time lag of EUV to $F_{10.7}$ results in an exaggerated ionospheric time lag effect to EUV when using $F_{10.7}$. Authors also report that the EUV–$F_{10.7}$ slope statistically tends to decrease when the SR variation of $F_{10.7}$ is significantly enhanced.

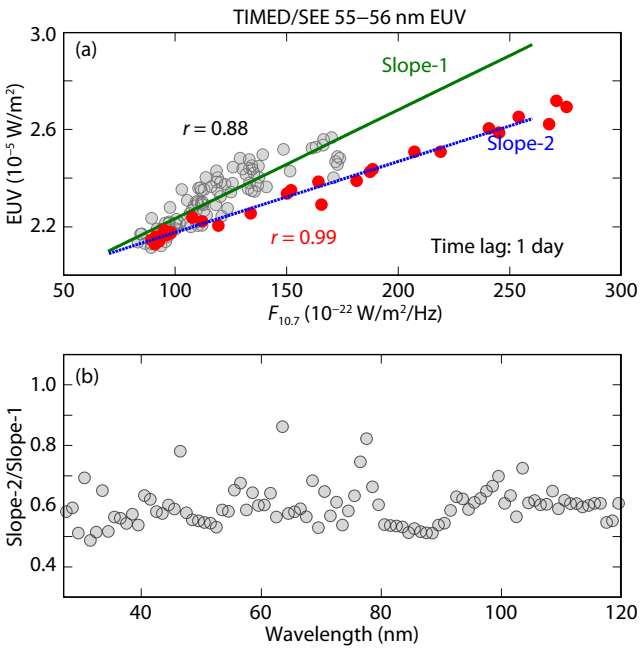

Figure 6. (a) Scatter plots of 55–56 nm EUV flux versus $F_{10.7}$. Red dots are the measurements during the 2008th–2009th CRs; for reference, gray dots present the measurements during adjacent CRs. The 1-day time lag effect of EUV to $F_{10.7}$ has been considered. The green solid line and blue dashed line are, respectively, the linear fittings for the grey dots and the red dots ("Slope-1" and "Slope-2" indicate their slopes); the parameter r is the correlation coefficient between EUV and $F_{10.7}$. (b) The ratios of "Slope-2" to "Slope-1" for different wavelengths. After Chen YD et al. (2018).

The ionosphere closely couples with the overlying plasmasphere at both sides of magnetic flux tubes. It is difficult to confirm interhemispheric coupling between the northern and southern mid-latitude ionosphere through the plasmasphere directly from observations. Interhemispheric conjugacy of the mid-latitude iono-

sphere, however, is a possible result induced by this coupling (Figure 7). Chen YD et al. (2019) reported an interhemispheric conjugate effect in longitude variations of mid-latitude ion density (N_i) using the Defense Meteorological Satellite Program (DMSP) measurements; northern and southern N_i longitude variations at dusk side are similar between magnetically conjugate mid-latitudes around solar minimum June Solstice. The conjugate effect occurs only inside the plasmapause where magnetic flux tubes are closed and the plasma in these tubes can stably corotate with the Earth. Neutral wind induced ionospheric transport causes topside longitude variations via upward diffusion at summer mid-latitudes; this further induces similar longitude variations of topside N_i at winter mid-latitudes via the summer to winter interhemispheric coupling. The conjugate effect not only proves mid-latitude interhemispheric coupling through the plasmasphere, but also implies that neutral wind induced transport can affect ionospheric coupling to the plasmasphere at mid-latitudes.

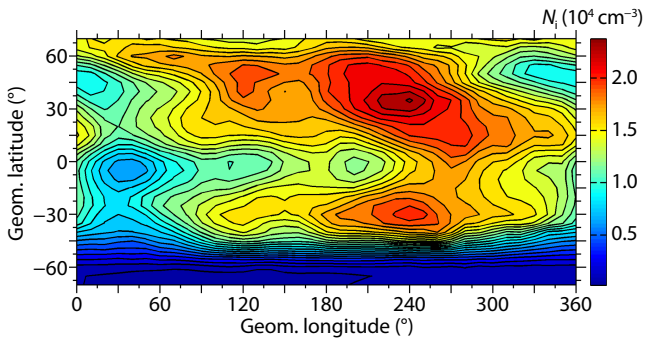

Figure 7. Geomagnetic longitude and latitude variations of the ion density at 840 km measured by the DMSP F_{12} satellite at nightside 21:30 LT around the June Solstice of 1996. After Chen YD et al. (2019).

Li QH et al. (2018) identified enhancements in nighttime ionization in the midlatitude ionosphere by using *in situ* electron density measurements from the CHAllenging Minisatellite Payload (CHAMP) and the DMSP satellites. The enhancements are found to be potentially connected to the plasmasphere with the magnetic flux tubes of L = 1.3–2.4, implying that the nighttime ionization enhancements may possibly be formed under coupling between the plasmasphere and the midlatitude ionosphere through downward plasma influx.

Global Navigation Satellite Systems (GNSS) and COSMIC radio occultation observations are widely used in ionospheric monitoring. Zhong JH et al. (2019a) revealed that the nighttime N_e at about ±40° geomagnetic latitudes is generally greater, especially in the topside ionosphere, during the solstices, at later local times at night and under lower solar activity, as referring to the middle-latitudinal bands (Figure 8). At these latitudes, the downward plasma diffusion from the plasmasphere provides a stable plasma source to the topside ionosphere, while the upward plasma motion due to the neutral winds is the primary source for the F_2 peak region.

Li ZX et al. (2019) revealed longitudinal variation characteristics of the ionospheric F_1 layer occurrence at middle- and high-latitudes in the daytime summer under low solar activity conditions using the COSMIC observations. Combined with the TIMED/GUVI observations and TIEGCM simulations, their analysis shows that the higher F_1 layer occurrence can be significantly affected by longitudinal variations of the O/N_2 ratios. The low O/N_2 ratios deplete the ionospheric electron density above the F_1 layer at middle and high latitudes and thus makes the F_1 layer stand out.

The state of the topside ionosphere has attracted more and more attention. Zhong JH et al. (2019b) used topside TECs observed by the MetOp-A and TerraSAR-X satellites for multiple local times to develop global topside ionospheric and plasmaspheric TEC models, based on empirical orthogonal function (EOF) analysis. The first five EOFs, which can account for more than 98.8% of the total variance, are applied in model construction. The comparisons indicate that the EOF TEC models can well reproduce the observations, including TEC magnitudes and longitudinal variations.

Yang N et al. (2018) statistically analyzed the mid-latitude trough position in the Northern and Southern hemispheres based on ion density data from the Defense Meteorological Satellite Program (DMSP) satellites in 1996–2016. The longitudinal variation of the trough position has significant seasonal, solar activity, and geomagnetic activity dependences. There are significant differences in the longitudinal variation of the trough position between the Northern and Southern Hemispheres.

Yang N et al. (2019) investigated the features of the high latitude trough in the Southern Hemisphere based on electron density, field-aligned currents (FACs), and ion drift velocity data from the Swarm-A satellite during 2013–2018. In the Southern Hemisphere the high latitude trough is a persistent post-midnight feature in winter, observed mainly in the eastern longitudes. They find a longitude dependence of features of FACs and ion drift velocity distribution in the high latitude trough region.

Zhang QH et al. (2018) reported *in situ* observations from a partial crossing of a reconnection layer near the subsolar magnetopause. During this crossing, step-like accelerating processes of the cold ions were clearly observed, suggesting that inflow cold ions may be separately accelerated by the rotation discontinuity and slow shock inside the reconnection layer (Figure 9). Cold ions of plasmaspheric origin have been observed to appear abundantly in the magnetospheric side of the Earth's magnetopause. These cold ions could affect magnetic reconnection processes at the magnetopause by changing the Alfvén velocity and the reconnection rate, they may also be heated in the reconnection layer during the ongoing reconnections.

Ding ZH et al. (2018b) presented some examples of the Qujing incoherent scatter radar (QJISR). The spectrum shape changes from a single hump to double humps with increasing altitude. The data reveal diurnal variations of ionospheric electron density, electron temperature, and ion temperature. The electron temperature at 200 km varies slowly during daytime and decreases quickly at sunset. The electron temperature near the peak height of the F_2 layer shows two peaks near sunrise and sunset. The ion temperature has no obvious diurnal characteristic.

Ding ZH et al. (2020) further investigated the electron temperature (T_e) of the ionospheric F layer by using Qujing incoherent scat-

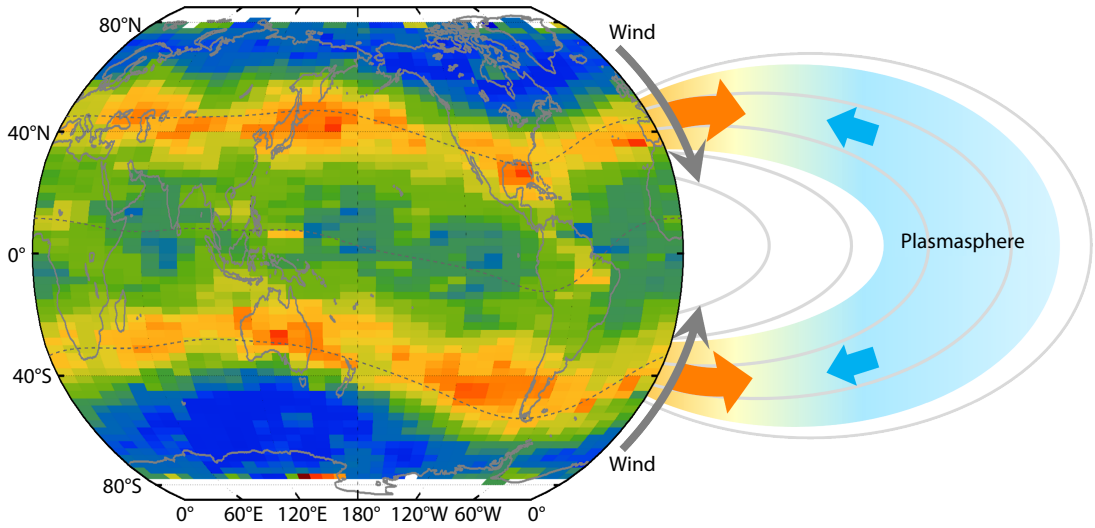

Figure 8. Newly discovered middle-latitudinal band structure in the nighttime topside ionosphere. The middle-latitudinal band structure at around ±40° geomagnetic latitudes is shown clearly in the electron densities at 800 km and 03 local time, which may be caused by plasma maintenance associated with equatorward neutral winds and downward ambipolar diffusion from the plasmasphere. After Zhong JH et al. (2019a).

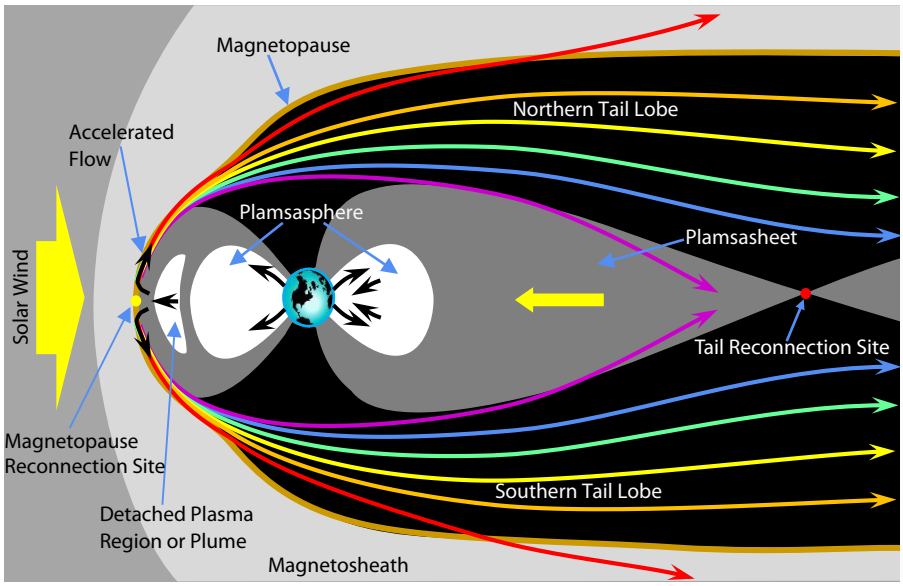

Figure 9. Schematics of ionospheric ion outflow. The brown line indicates the magnetopause (the outer boundary of the magnetosphere), inside which are three distinct regions: (1) the tail lobes (black) contain "open" magnetic field lines threading the magnetopause that are generated in the Dungey cycle during periods of southward IMF by magnetic reconnection at the dayside magnetopause (at the yellow dot) and re-closed by reconnection in the tail (at the red dot); (2) the plasma sheet (dark grey) contains closed field lines that connect the ionospheres in the two hemispheres and never thread the magnetopause; these closed field lines convect sunward in the Dungey cycle; (3) the plasmasphere (in white) is also on closed field lines and has higher plasma densities than the plasmasheet because magnetic flux tube volumes are smaller and can be filled by outflows from the ionosphere. The colored lines show trajectories for ions of plasmaspheric origin from the reconnection acceleration region. Note that all ions are moving along the magnetic field lines but trajectories are not field-aligned because the field lines move as part of the Dungey convection cycle. Higher energy ion trajectories (red arrows) are closer to field aligned than lower energy ones (in mauve) because they have higher field parallel velocities. After Zhang QH et al. (2018).

ter radar (QJISR) measurements in 2017 and 2018. T_e increases from about 150 km, reaches its maximum at about 220 km, then decreases and reaches its minimum at 300–350 km. T_e above the F_2 peak height has morning and sunset enhancements with maximum value at about 3000 K. The sunset rise of T_e occurs earlier at higher altitudes. T_e and electron density (N_e) have a positive correlation below 200 km and a negative relationship between 200 and 450 km.

Yang SG et al. (2019) investigated two cases of F_2-lacuna and their

simultaneous ionospheric convection and TEC variations at Zhongshan Station (69.4°S, 76.4°E, corrected geomagnetic latitude 74.5°S). The two cases of F_2-lacuna are accompanied by a decrease of electron density and an increase in plasma flow. They propose that the strengthened electric field brings Joule heating and frictional heating, which enhances the electron and ion temperatures. Subsequently, the enhancement of the recombination rate and the O^+ upflow results in a decrease of O^+ density in the F_2 region.

Zhang KD et al. (2018) investigated longitudinal patterns of middle and low latitude zonal thermospheric winds, using CHAMP observations and TIEGCM modeling. Their results show that there are large longitudinal variations in zonal thermospheric winds, exhibiting no significant solar activity dependence. The geomagnetic configuration is the main agent of longitudinal changes in the zonal wind. Furthermore, the zonal wind shows great hemispheric asymmetry, and local time and seasonal variations.

3. Ionospheric Dynamics and Couplings

The dense oblique-incidence ionosonde network in North China makes it possibly to monitor ionospheric regional variations with high spatial resolution. Chen G et al. (2018) used the network to investigate ionospheric nighttime oscillations in January and February 2011. Opposite latitudinal dependences are present in the premidnight and postmidnight enhancements in electron density. The premidnight enhancements appeared earlier at higher latitudes and then moved to lower latitudes, as a part of the large-scale travelling ionospheric disturbance (LSTID) being produced by gravity waves. The LSTIDs is considered to form the positive latitudinal dependence of the wave peaks and troughs. The postmidnight oscillation was observed to have a peak and a trough. The most likely agent is the westward electric field-induced $\boldsymbol{E}\times\boldsymbol{B}$ drift, which pushed the F layer to lower altitudes.

A solar eclipse provides a great opportunity to explore the basic physics of the ionosphere–thermosphere (I–T) system. Dang T et al. (2018a) and Lei JH et al. (2018b) investigated the global dynamic and electrodynamic responses of the ionosphere and thermosphere to the 2017 solar eclipse, using a high-resolution global coupled ionosphere–thermosphere–electrodynamics model. They found that the I–T response to the eclipse was global and long-lasting, not local as previously expected. The ionosphere and thermosphere showed significant global changes (Figure 10), even more than a half day after the conclusion of the eclipse. Furthermore, an evident suppression of the TOI was reported by Dang T et al. (2018b) when the eclipse occurs in the afternoon sector at middle latitudes, due to the electron density reduction in the middle latitude source region.

Sun YY et al. (2018b) analyzed the massive total electron content (TEC) observations from 2255 ground-based Global Navigation Satellite System (GNSS) receivers on the continent of United States (CONUS) during the total solar eclipse on 21 August 2017. The results show that the moon shadow (~80% obscuration) generates a great ionospheric bow wave (period < 10 minutes) which extends ~1500 km away from the totality path. The bow wave consists of the acoustic shock wave due to the supersonic/near-supersonic moon shadow "ship" and the significant plasma recombination due to the reduction in solar irradiation within the shadow area. The bow-wave crest in front of the totality is most intense as the moon shadow moves over the northwest coast of the CONUS, where the shadow is supersonic (~1000 m/s). The crest decreases by 80% when the boat velocity reduces to the speed of sound (~650 m/s), on the eastern coast.

After suggestions that greenhouse gases may have effects on the ionosphere, ionospheric climate study received considerable attention and funding. Recently, the Wuhan ionosonde observa-

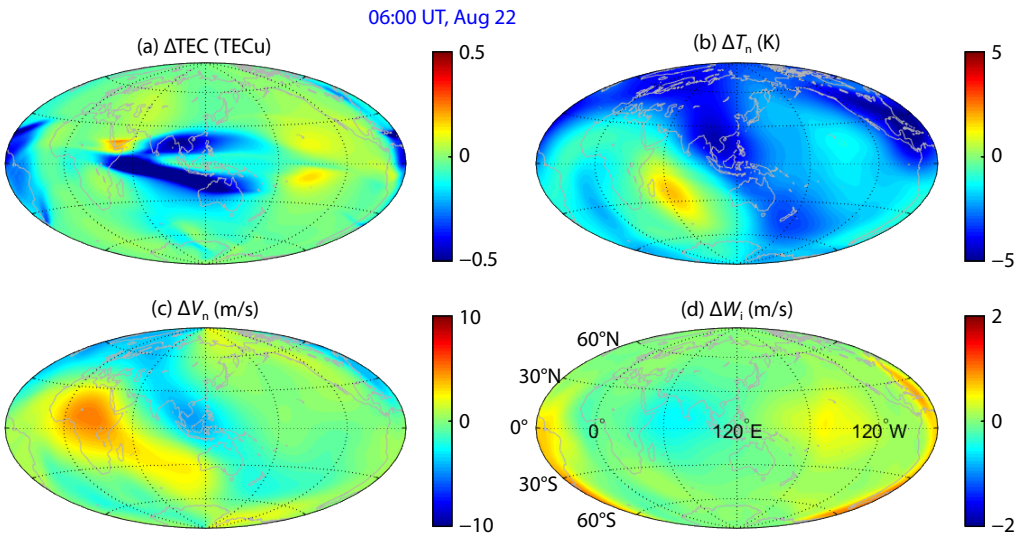

Figure 10. Global maps of differential TEC, neutral temperature, meridional winds (northward positive), and $\boldsymbol{E}\times\boldsymbol{B}$ vertical plasma drifts (upward positive) at pressure level 2 (~300 km) between the model simulations with and without eclipse at 06:00 UT on 22 August 2017, 9 hours after the final contact of eclipse. The solar eclipse is a transient local event, but its impact on the ionosphere and thermosphere can persist for a considerable time over the entire globe, rather than just being an impulse event with a localized response as was previously expected. After Lei JH et al. (2018b).

tions back to 1947 were digitized and standardized through a unified method. Yue XX et al. (2018) used the Artificial Neural Network (ANN) to analyze the long term trend of these Wuhan data and found mean f_oF_2 and h_mF_2 trends of −0.0021 MHz/a and −0.106 km/a, respectively. They investigated further the effects of CO_2 and geomagnetic field strength, using data from the NCAR-TIEGCM driven by Mauna Loa Observatory (observed CO_2 levels) and International Geomagnetic Reference Field (IGRF) (geomagnetic field) to simulate their effects on ionospheric long-term trend over Wuhan. Simulation results show that CO_2 and geomagnetic field have comparable effect on h_mF_2 trends, while on the f_oF_2 trend over Wuhan the geomagnetic field effect is stronger than that of CO_2. Both factors result in obvious but different diurnal variations of f_oF_2/h_mF_2 long-term trends. The geomagnetic field effect is nonlinear versus years since the long-term variation of geomagnetic field intensity and orientation is complex. Regarding the diurnal variation of the trend, the simulation accords well with that of observations except for h_mF_2 results around 12 UT. Overall, good agreement between observation and simulation illustrates the good quality of Wuhan ionosonde long-term data. Furthermore, little attention has been paid to the topside ionosphere. Cai YH et al. (2019) used the series Defense Meteorological Satellite Program (DMSP) satellites since 1987 to derive the long-term trend of the topside ionosphere for the first time. The electron density (N_e) trend from 1995–2017 in the middle and low latitudes at ~860 km around 18 MLT was derived using the ANN method. The trend from DMSP observations has a mean magnitude ranging from ~ −2% to ~2% per decade, with clear seasonal, latitude, and longitude variations. The derived trend was evaluated by direct comparison with the simulated trend at 500 km from the NCAR-TIEGCM data driven by realistic changes of CO_2 level and geomagnetic field. The observed and simulated trends have similar geographic distribution patterns at 18 MLT. The good agreement between the observed trend around 860 km and the simulated trend near 500 km implies that the physical processes controlling the N_e trends above the peak height might be identical. Further controlled simulations show that the geomagnetic field secular variation, rather than the CO_2 long-term enhancement, is the dominant factor in the electron density trend at around 500 km.

Chen T et al. (2019) developed a new method, based on IGS TEC and TIMED wind data, to interpret the atmospheric contribution to the ionospheric wave number-4 (WN4) structure according to their coherences in annual variations. They confirmed previous suggestions that symmetric zonal DE3 is the primary source for ionospheric WN4, and that the contributions due to antisymmetric wind components are relatively small in TEC WN4.

Mo XH and Zhang DH (2018) investigated the longitudinal dependence of periodic meridional movement of EIA crest during sudden stratospheric warming events in 2003, 2006, and 2009 by using GPS TEC observations in the Chinese and Brazilian sectors. The locations of EIA crests in the two sectors exhibit in-phase 14- to 15-day periodic oscillations that, coincide with half of the lunar revolution period (29.53 days) and the lunar phase; this temporal feature is consistent with that of stratospheric zonal wind.

Liu J et al. (2019b) further studied the longitudinal differences in low-latitudinal TEC responses in winter between the East Asian and American sectors. The analysis suggests that the M2 effects on the low-latitudinal ionosphere during SSWs are likely to be more prominent in the American sector than in the East Asian sector. These differences probably result from a combined effect of the longitudinal variety in atmospheric (especially tidal) and electrodynamic processes.

The physical mechanism of the ionospheric electric field has not been well understood. Chen JJ and Lei H (2019) found that the altitudinal and latitudinal variations of zonal electric fields are associated with latitudinal variations of meridional winds, longitudinal gradients of zonal winds, and the global nature of the dynamo process. Moreover, when neutral winds affect electric fields by wind dynamo, the $\boldsymbol{E}\times\boldsymbol{B}$ drifts caused by electric fields can drag thermospheric winds as well. The interaction of electric fields and neutral winds will result in the relationship between field-aligned and field-perpendicular plasma velocities in the ionospheric F region (Chen JJ and Lei JH, 2019).

The polar ionosphere–thermosphere system is a crucial part of space weather; it directly connects the solar wind-magnetosphere and the lower atmosphere. Based on high-resolution Thermosphere Ionosphere Electrodynamics General Circulation Model (TIEGCM) simulations as well as on DMSP satellite observations, Dang T et al. (2019) have reported the occurrence of double Tongues of Ionization (TOIs) (Figure 11) and carried out a comprehensive study of the dynamic evolution and formation mechanism of double TOIs. Predicting the cusp electron precipitation is important in investigating the dayside solar wind-magnetosphere–ionosphere coupling process and in forecasting space weather phenomena. Dang T et al. (2018c) used the global MHD simulation to investigate the correlation between the fluxes of precipitating electrons in the cusp and the upstream solar wind conditions. The statistical results indicated that both the hemispheric precipitation rate and the hemispheric power of precipitating soft electrons are closely correlated with solar wind dynamic pressure.

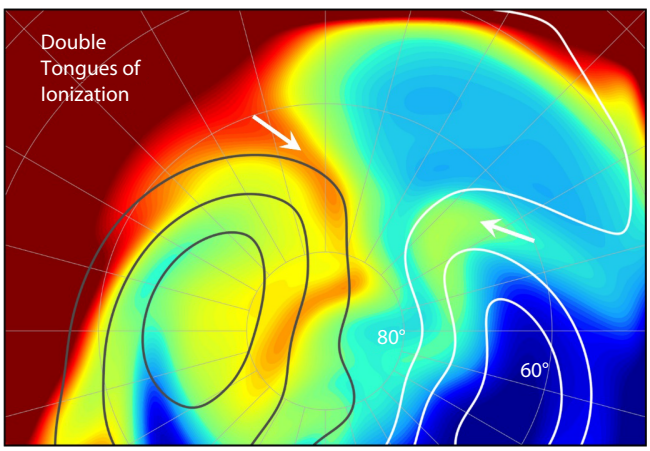

Figure 11. Polar map of simulated electron densities as a function of local time and geographic latitude at 10:00 UT during the March 17 2013 geomagnetic storm. The results clearly show that two TOIs existed within dawn and dusk convection cells. After Dang T et al. (2019).

Wu YW et al. (2019) analyzed the universal time (UT) variations of the polar ionosphere (Figure 12) in terms of the mean polar electron content, based on COSMIC observations. They report that the UT variation has stronger intensity in the Antarctic than in the Arctic, their phases differing by 12 hours. The main driver of the polar ionosphere's UT variation is the varying convection pattern, in geographic coordinates.

Guo DJ et al. (2019) used the Global Ionosphere–Thermosphere Model (GITM) to simulate the isolated density cell in the high-latitude thermosphere. They suggest that the downward wind and ion drag-driven force should lead to density depletion or a low density cell. Further, Weng LB et al. (2019) invested the climatological view of density cell structures at high latitudes in the lower thermosphere, using neutral mass density at 270 km derived from the GOCE (Gravity Field and Steady-State Ocean Circulation Explorer) satellite. They found that density cell structures in the lower thermosphere tend to occur in the local summer and the northern hemisphere, and that their local time distributions, horizontal scales, and relative magnitudes depend on the type of density cell structure. Weng LB et al. (2018) further discussed the seasonal variations of lower thermospheric density by using GOCE satellite data and the Empirical Orthogonal Function method. They found that the seasonal density variations show obvious hemispheric asymmetry, with large amplitudes in the southern hemisphere, and that the annual asymmetry and effect of the Sun–Earth distance vary with latitude and solar activity.

The thermospheric temperature is an important parameter for both physics understanding and space weather prediction. Ruan HB et al. (2018) revealed and quantified the potential impact of satellite sampling on dynamical modeling of the thermosphere. They found a significant reduction of the relative deviation by blending data from more than one satellite. Based on observations and numerical simulations, Ruan HB and Lei JH (2019) developed an empirical temperature model via data-driving technology, for the purpose of dynamical correction in thermospheric determination. Ren DX et al. (2019) investigated the thermospheric responses to the 27-day variation of solar EUV flux. They found that the 1-day peak response time of the thermospheric temperature to the periodicity of solar EUV flux corresponds to the balance between the heating and cooling processes, and that this delay is modulated by the circulation.

Owolabi et al. (2019) studied the driving forces of the EEJ current, tidal variability in EEJ current, counter equatorial electrojet (CEJ) current, and ionospheric electric current system during two major SSW events (2006 and 2009) at three different longitude sectors. They found that during SSW events the tidal components are responsible for modulating ionospheric currents. The tidal component in EEJ strength during an SSW event is associated with significant reduction and enhancement in EEJ strength.

The enhancement in EEJ could modulate directly the variations of the ionosphere. Liu GQ et al. (2019) analyzed characteristics of the TEC (Figure 13) recorded at middle- and low-latitude stations over the Chinese sector during the 2018 SSW event. The deviation of TEC from its mean exhibits strong semi-diurnal and diurnal oscillations, and the EEJ shows a significant correlation with peak TEC in the low latitude region, illustrating the energy transmission and coupling between the lower atmosphere and the ionosphere.

Sun YY (2019) summarized recent studies of the effect of solar (geomagnetic storm and total solar eclipse), tropospheric (typhoon, walker circulation, and El Niño–Southern Oscillation), and earthquake/tsunami activities on the ionosphere, utilizing global ground- and space-based GNSS observations. Solar activities from above and perturbations of Earth's surface and troposphere from below both disturb ionospheric structure and its dynamics. Numerous ionospheric phenomena remain unexplained due to the complicated nature of the solar-terrestrial environment. Techniques and high resolution global observations from the ground- and space-based Global Navigation Satellite System (GNSS) will help us to resolve unexplained phenomena.

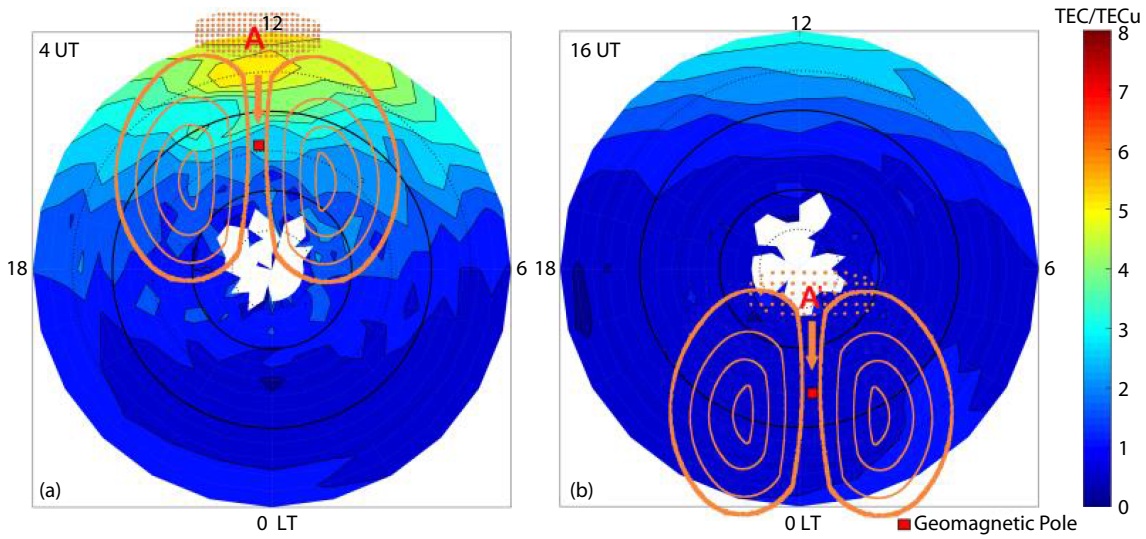

Figure 12. The TEC maps at (a) 4 UT and (b) 16 UT in winter in the Antarctic, in geographic coordinates. The red square gives the location of the magnetic pole in the southern hemisphere. The orange circles and the dots are schematic diagrams, standing for the convection electric fields and the electron densities, respectively. After Wu YW et al. (2019).

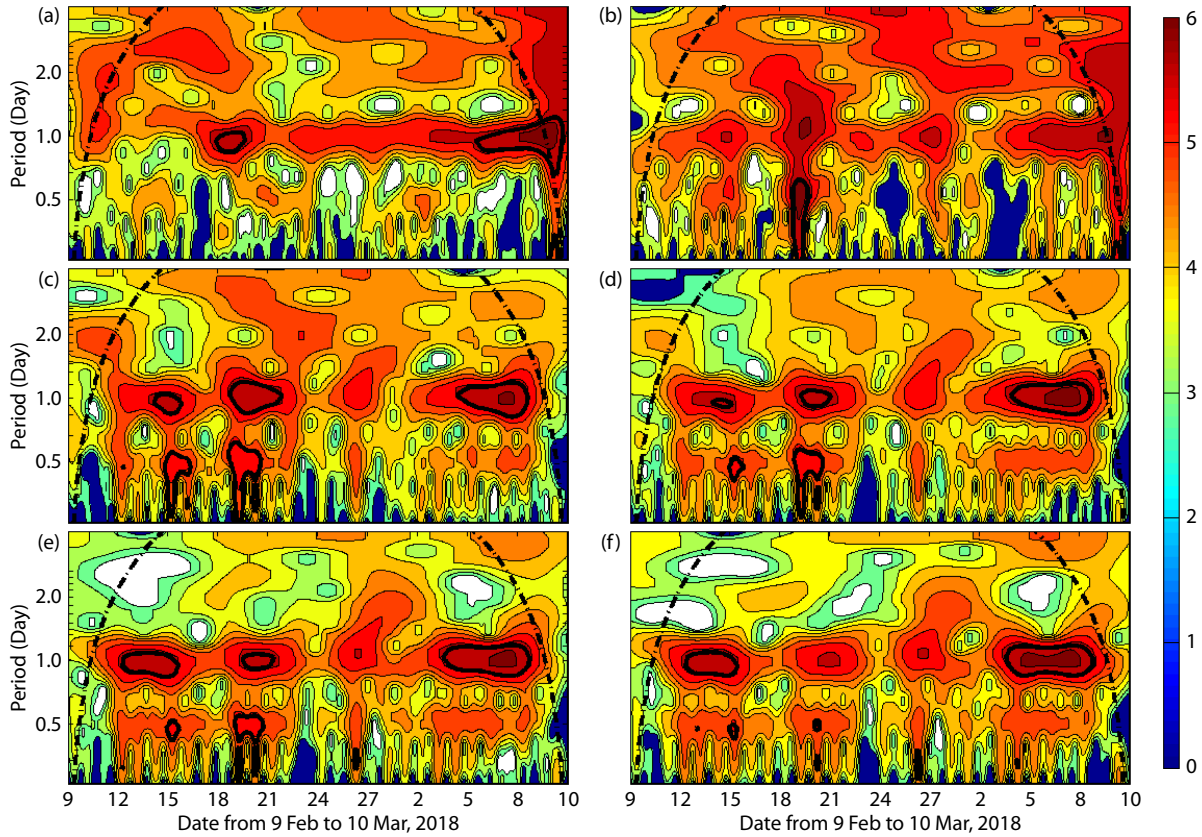

Figure 13. Continuous wavelet power spectra of the deviation of TEC from its mean for (a) Mohe, (b) Beijing, (c) Xiamen, (d) Guangzhou, (e) Nanning, and (f) Kunming. The solid black curves designate the 5% significance level. The dashed lines are the cone of influence. After Liu GQ et al.(2019).

To better understand the ionospheric morphology response to possible lithospheric activities, Sun YY et al. (2019b) examined the global location preference of positive and negative TEC anomalies that persist continuously for longer than 24 hours at middle and low latitudes (within ±60°N geomagnetic latitudes). Less than 4% of TEC anomalies meet this criterion. The conjugate phenomenon of TEC persistence is most significant in the longitudinal sector of eastern Asia to Australia. Their result shows persistence of the positive TEC anomaly along the ring of fire on the western edge of the Pacific Ocean. The high persistence of the TEC anomalies at midlatitudes suggests that thermospheric neutral wind contributes to the anomaly formation.

Sun YY et al. (2019a) examined the influence of the El Niño–Southern Oscillation (ENSO) on the ionospheric TEC DE3 (diurnal eastward wavenumber 3) and SPW4 (stationary planetary wavenumber 4) which are major components of the ionospheric wave-4 longitudinal structure. The TEC is the integration of electron density from 200 km to 800 km, sounded by the GPS radio occultation (RO) experiment onboard the FORMOSAT-3/COSMIC satellites during the period of January 2007–December 2015. Their results show that the TEC DE3 and SPW4 amplitudes respond to the ENSO signature in the thermospheric wind DE3 in the Northern Hemisphere during the lower solar activity period. The 2010/2011 strong ENSO cold phase significantly enhances the TEC DE3 and SPW4 amplitudes with periods from 1 year to quasi-biennial periodicity at low latitudes of the Northern Hemisphere. The QBO crests of the TEC DE3/SPW4 and the wind DE3 at lower thermosphere were almost in phase during the 2010/2011 ENSO cold phase.

Sun YY et al. (2018a) studied the El Niño–Southern Oscillation (ENSO) signals in the two dominant temperature diurnal tides, DW1 (diurnal westward wavenumber 1) and DE3 (diurnal eastward wavenumber 3), on the quasi-biennial oscillation (QBO) scale (18 to 34 months) from 50 km to 100 km altitudes. The tides are derived from the 21-year (January 1996 to February 2017) GAIA (Ground-to-topside model of Atmosphere and Ionosphere for Aeronomy) temperature simulations and 15-year (February 2002 to February 2017) TIMED (Thermosphere Ionosphere Mesosphere Energetics and Dynamics) / SABER (Sounding of the Atmosphere using Broadband Emission Radiometry) temperature observations. The GAIA simulations and SABER observations show that the ENSO controls the QBO in the stratosphere, mesosphere, and lower thermosphere. ENSO warm phases shorten the period (~2 years) of the QBO in DW1 amplitude near the equator and of the DE3 amplitude at low latitudes of the Northern Hemisphere. In contrast, the QBO period lengthens (~2.5 years) during the ENSO neutral and cold phases. Correlation analysis revealed that the ENSO effect on the tidal QBO can last more than one year in the mesosphere and lower thermosphere.

Wang H et al. (2018) investigated the temporal and spatial variations of thermospheric neutral winds at 400 km altitude under the influence of subauroral polarization streams (SAPS) based on

simulations of the global ionosphere and thermosphere model (GITM). During SAPS periods under southward IMF conditions, the westward neutral winds at subauroral latitudes are greatly strengthened at dusk. The strongest westward neutral winds exhibit large variations in amplitudes when SAPS commence at different universal times.

Wang H et al. (2019) used 10 years of CHAMP observations to investigate how the counter equatorial electrojet (CEJ) depends on interplanetary magnetic field (IMF) conditions. The longitudinal distribution of the equatorial electrojet (EEJ) is closely modulated by the solar zenith angle. The correlation between EEJ intensity and the square root of the average value of cos (SZA) during CEJ events becomes stronger around the June solstice. Compared to normal conditions, CEJ occurrences were found to double during subauroral polarization stream periods.

The radio occultation (RO) technique is a useful tool for detecting atmospheric waves induced by earthquake/tsunami events. Yan XX et al. (2018) examined the FORMOSAT-3/COSMIC RO soundings of TEC in the ionosphere (from 150 to 550 km) and the refractivity index in the lower atmosphere (from 0 to 60 km) after/during the 2011 M_w9.0 Tohoku earthquake/tsunami. Their results show that the atmospheric oscillations with vertical wavelength ranging from 0.5 to 8 km and from 10 to 40 km, respectively, appeared in the stratosphere and ionosphere after the earthquake's onset. These atmospheric oscillations were also identified after the 2008 M_w7.9 Wenchuan earthquake. The interesting point is that these atmospheric oscillations can also excite secondary oscillations in the solid Earth, as exhibited in ground seismic data (Yan XX et al. 2020).

Liu Y et al. (2019a) investigated effects on the ionosphere of an underground nuclear explosion (UNE) — the nuclear test of North Korea in 2017 — by using data from IGS stations and Swarm satellites collected simultaneously with the explosion. Geomagnetic conjugate ionospheric TEC disturbances were observed. They propose that the observed UNE-generated ionospheric TEC disturbances are results of electrodynamic processes caused by LAIC (Lithosphere–Atmosphere–Ionosphere Coupling) electric field or electric current penetration.

4. Ionospheric Irregularity and Scintillation

The polar region opens a natural window to space. Its various irregularities include patches in the polar ionosphere. The plasma patches are usually linked to ion upflow. Data from instruments aboard the Global Navigation Satellite System (GNSS) are often degraded during the formation and evolution of multiple-scale plasma irregularities, especially when combined with simultaneous particle precipitation. Jin YY et al. (2019) performed a statistical analysis of 345 dayside patches observed by the EISCAT Svalbard Radar from 2010 to 2013. They report that polar cap patches are formed preferentially under southward IMF conditions. There is a clear B_y-related IMF asymmetry in their dependence on magnetic local time (MLT). The pulsed dayside magnetic reconnection is proposed to be possibly a significant mechanism of polar cap patch formation.

Xing ZY et al. (2018) reported a case of conjugate polar cap arcs on 5 Feb 2006 (Figure 14), observed by the ground-based all-sky imager at Yellow River Station (Svalbard) and by the space-based DMSP/SSUSI and TIMED/GUVI instruments. The movement of the polar cap arc shows a clear dependence on the interplanetary magnetic field (IMF) B_y component, moving from dusk to dawn in the northern hemisphere and vice versa in the southern hemisphere. Strong flow shears are observed around the polar cap arc in both hemispheres. It is reasonably expected that the topological changes in the magnetotail can produce a strip of closed field lines. Local processes would set up conditions for formation and evolution of polar cap arcs.

Wang Y et al. (2018) analyzing GPS measurements of the ionospheric plasma flow, from SuperDARN radars around the noon sector of polar ionosphere, reported that the phase scintillation index exhibits a strong linear dependence on the plasma drift speed, whereas the amplitude scintillation index does not present such a dependence, implying that the phase scintillation index is much more sensitive to plasma flow. This observation is explained as a consequence of Fresnel frequency dependence of the relative drift and of the choice of a cutoff frequency (0.1 Hz) to detrend the data for obtaining standard phase scintillation index. Care must be taken when attempting to distinguish between phase scintillation (diffractive) phase variations and refractive (deterministic) phase variations, especially in the polar region where the ionospheric plasma drift is much larger than in equatorial and midlatitude regions.

Priyadarshi et al. (2019) identified the orientation of ionospheric irregularities over Weihai with the local geomagnetic field by using the phase screen model and wave propagation theory in random media. Amplitude and phase scintillation data from the GNSS receiver deployed at the mid-latitude observation station Weihai were used along with the *K*-index derived from the horizontal magnetic field component of the local magnetometer. The proposed model uses the relationship between scintillation indices and local *K*-index, finding a scintillation dependence over local *K*-index during geomagnetic quiet and disturbed condition.

Ma YZ et al. (2018a) investigated ion upflow occurrence, speed, density, and flux above the polar cap in the northern hemisphere under different solar zenith angle, solar activity ($F_{10.7}$), and convection speed by analyzing a five-year period (2010–2014) of DMSP plasma data. High upflow occurrence rates in the dawn sector are associated with regions of higher convection speed, while higher upflow flux in the dusk sector is associated with higher density. The upflow occurrence increases with convection speed and solar activity but decreases with SZA. Upflow occurrence is lowest when the SZA > 100° and convection speeds are low. Upflow velocity and flux show a clear seasonal dependence — higher speed in the winter and higher flux in the summer during low convection conditions; however, during high convection conditions in summer, both speed and flux are observed to be higher. The ion upflow in the polar cap region appears to be is suggested to be controlled by a combination of convection, solar activity, and solar illumination.

Ma YZ et al. (2018b) investigated the characteristics of hot patches versus classical patches by using a five-year database of *in situ* plasma observations from DMSP satellites. The vertical ion flux is

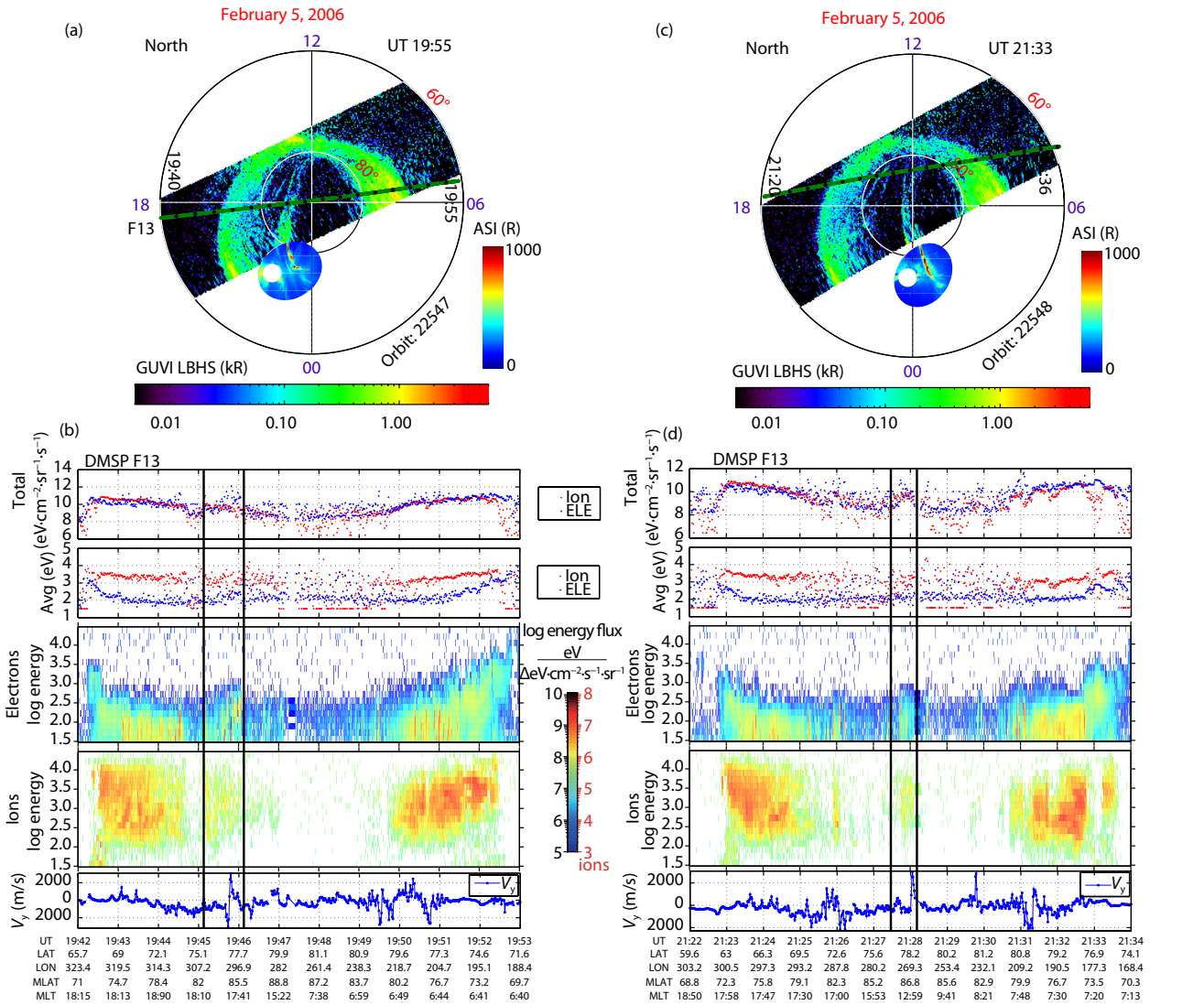

Figure 14. (a) and (c) TIMED/GUVI data superimposed on the 557.7 nm ASI data at 19:55 UT and 21:33 UT, and the overpass of DMSP F13 crossing the PCA superimposed on the image, shown in MLAT/MLT coordinates. The white spots duskside of the PCA on the ASI image are used to cover the moonlight. (b) and (d) Data from a DMSP F13 pass during the intervals from 19:39 to 19:56 UT and from 21:00 to 21:37 UT. The spectrogram includes (top to bottom) integral energy flux, average energy, spectra of precipitating electrons and ions, and velocity of cross-track horizontal plasma drift. The vertical black lines mark the times when DMSP F13 passed over the PCA. After XING ZY et al. (2018).

generally downward in classical patches ($T_i/T_e > 0.8$ or $T_e < T_i + 600$ K), and generally upward in hot patches ($T_i/T_e < 0.8$ or $T_e > T_i + 600$ K). Thus, the ion/electron temperature ratio can be used as a parameter to identify classical and hot patches. The highest upflow occurrence was found near the polar cap boundary, associated with hot patches, particle precipitation, strong convection speed, and localized field-aligned currents. The polar cap hot patches may play a very important role in solar wind–magnetosphere–ionosphere coupling processes.

The storm-time variation of ionospheric equatorial plasma bubbles (EPBs) and their associated driving mechanisms can be highly complicated. Aa et al. (2018a) first reported a unique observation of postsunset super EPBs over China and adjacent areas during the second main phase of the geomagnetic storm on 7–8 September 2017. Moreover, Aa et al. (2019) also observed similar postsunset super EPBs over the American sector during the first main phase of the same geomagnetic storm on 7–8 September 2017. In both cases, signatures of EPBs could be observed from the following measurements: (1) prominent stream-like structures of depletion (~5–15 TECU) in GNSS TEC and irregularities in ROTI maps, (2) severe plasma bite-out of 2–3 orders from the Swarm/DMSP N_e profiles, and (3) significant enhancement of F-layer height and vertical drifts. The ionospheric irregularities were registered for ~5 hour and reached as far as 45° Magnetic Latitude in both Asian and American sectors.

Furthermore, Aa et al. (2020) presented coordinated and fortuitous ground-based and spaceborne observations of EPBs, combining the Global-scale Observations of Limb and Disk (GOLD) far ultraviolet emission images, GNSS TEC data, and Swarm *in situ* plasma density measurements. These multi-instrument measurements (Figure 15) provide an effective way to illustrate an integrated and comprehensive image for specifying both large-scale

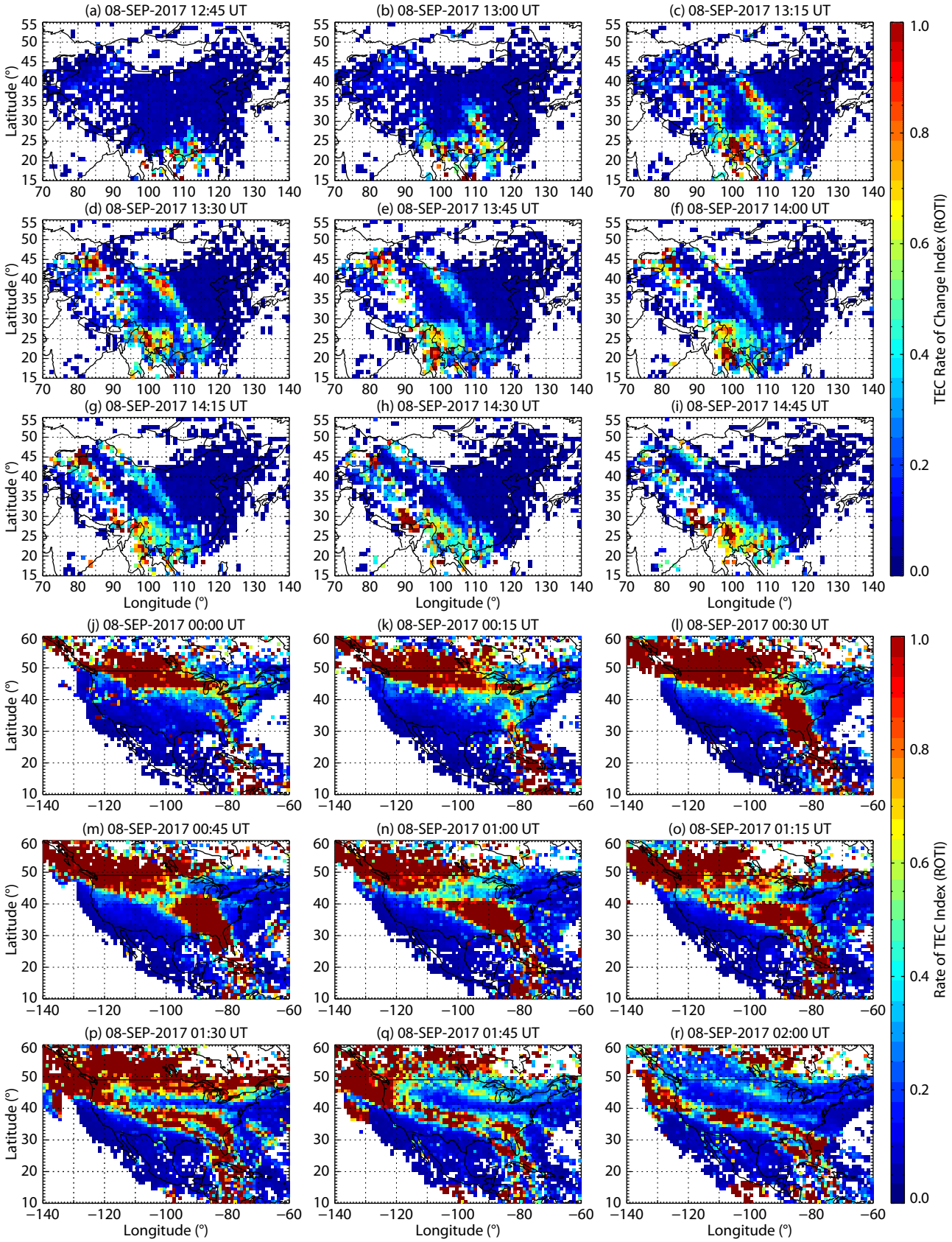

Figure 15. TEC rate of change index (ROTI) maps of ionospheric irregularities over (upper) East Asian and (lower) North American sectors, respectively. Adapted from Aa et al. (2018a) and Aa et al. (2019).

and mesoscale features of EPBs.

In recent years, an international space weather meridian circle program, using diverse instruments along the approximate meridian 120°E/60°W, that is, the Asian and American longitude sectors, was launched with the goal of providing a global picture of unfolding space weather events. Li GZ et al. (2018c) reported a unique case, during the September 2017 geomagnetic storm sequence, of significantly enhanced postsunset EPBs developments by prompt penetration electric field (PPEF) in both the American and Asian sectors, but their total absence by disturbance dynamo electric fields in the Pacific sector. The PPEF induced EPBs along the meridian showed different characteristics, with an apparent west-tilted structure in the Asian sector that was not apparent in the American sector. This sort of study based on the international space weather meridian circle program observations would strengthen the understanding of the generation and evolution characteristics of EPBs during geomagnetic storms.

The fresh generation of equatorial plasma bubbles (EPBs) is usually a nighttime phenomenon. Li GZ et al. (2018a) reported an unexpected case of daytime F-region irregularities freshly generated following the appearance of an ionospheric hole over low latitudes on May 30, 2016. The irregularities developed initially around 10:57 LT above the F-region peak height (~360 km), with a thickness of about 30 km and an east-west extension of more than 200 km, and then expanded upward to 500 km altitude behaving like the EPB irregularities of the nighttime ionosphere (Figure 16). Based on the coincidence, both in space and time, with the appearance of an ionospheric hole, which was generated after the passage of a rocket, they concluded that the daytime F-region irregularities must have been artificially generated locally through a manifestation of plasma instability triggered by the rocket exhaust-induced ionospheric hole over low latitudes. Their results provide solid evidence of the possibility of artificial triggering of EPB irregularities.

The coupling of equatorial and low-latitude ionosphere has been an active area of research for many years. By using Sanya (18.4°N, 109.6°E, dip latitude 12.8°N) VHF radar and ionosonde observations during equinoctial months of 2012–2016, Xie HY et al. (2018) statistically investigated occurrences of post-sunset ionospheric E, valley, and F region irregularities, the postsunset rise of F layer, and their correlations. Their results reveal a statistically significant correlation between the presence of valley region irregularities (VRIs) and initial development of EPBs. They suggest that the electrodynamic processes associated with EPB development and ionospheric background electric field contribute significantly to the generation of E region irregularities (ERIs) and VRIs over Sanya. The mapping of polarization electric fields (PEFs) generated within the fresh EPB structure could enhance (inhibit) the generation of VRI (ERI) over Sanya. The occurrence peak of ERI around 11:00 UT, however, could be due to the mapping of downward electric field above the equatorial plasma vortex shear node.

The small-scale wave-like structure (SSWS) of plasma density in the bottomside F region was proposed to be an important seeding for equatorial plasma bubble (EPB) generation. Although the seeding role of SSWS has been reproduced in theoretical simulations of EPBs in recent years, confirmatory observations of the phenomenon have been lacking. Liu KK et al. (2019) reported two large-scale wave-like structures (LSWSs) that were closely situated in longitude by using Fuke all-sky airglow imager (19.3°N, 109.1°E; dip latitude 14.3°N) observations. The LSWSs were amplified and drifted eastward during the sunset pre-reversal enhancement of zonal electric field. Two SSWSs appeared later in the western LSWS and subsequently developed into an EPB. For the eastern LSWS, no SSWS and EPB were observed. Their results could provide supporting evidence for SSWS seeding of EPBs.

Based on multi-instruments observations, Luo WH et al. (2018) studied the possible physical processes controlling low-latitude plasma density enhancements, which are also referred to as plasma blobs. Their results indicate that the meridional wind plays an important role in the formation of plasma blob in low-latitude regions.

Yu T et al. (2018a) studied solar activity variation of global equatorial F region irregularities (EFIs) using the data of the COSMIC *S*4 index profiles. The occurrence rates of EFIs at higher altitudes (greater than 500 km) show a clear solar activity dependence, while total occurrences at the entire range of altitudes (from 150 to 800 km) do not have clear relationship with solar activity. The solar activity sensitivity of the occurrence rates of EFIs is strongest at equinoxes and weakest in summer.

Yu T et al. (2018b) developed a new method for estimating motions of equatorial plasma bubbles (EPBs) from airglow emission all-sky images. The method can determine the velocity of different parts within EPBs, after considering the EPBs' deformation.

Wu K et al. (2018) showed a feature related to equatorial plasma depletions by using four years (2012–2015) of observations of the all-sky imager and C/NOFS satellite. The edge plasma enhancements of equatorial plasma depletions (EPEEPDs) is a high-incidence phenomenon, with a rate as high as 82%. The zonal extension of EPEEPDs has scale characteristics varying with altitude. The generation mechanism of EPEEPDs is possibly related to the polarized electric field of EPDs.

Wang Z et al. (2019) reported three cases of concurrent plasma blobs and bubbles around 22:30 LT in the same magnetic meridian in the Asian-Oceanian sector during solar maximum, in terms of simultaneous observations from in-situ satellite and ground ionosonde/GPS scintillations at Vanimo station (geog. 2.7°S, 141.3°E; geom. 11.2°S, 146.2°W) and at Hainan station (geog. 19.5°N, 109.1°E; geom. 9.1°N, 179.1°W). Magnetic field line mapping shows that the blobs in these two cases were at equatorward and above bubbles, providing direct observational evidence for blob formation in the intermediate stage of plasma bubble evolution.

Zhang M et al. (2019) studied the temporal and spatial distribution of the amplitude scintillation at Shenzhen. They report that the amplitude scintillation occurs mainly after sunset and lasts until midnight in equinox months. The loss of lock (LoL) of GPS signals at HKSL, a nearby GPS station, exhibits a temporal variation very similar to that of the amplitude scintillation. The scintillation and LoL occur more frequently in the southern part of Shenzhen.

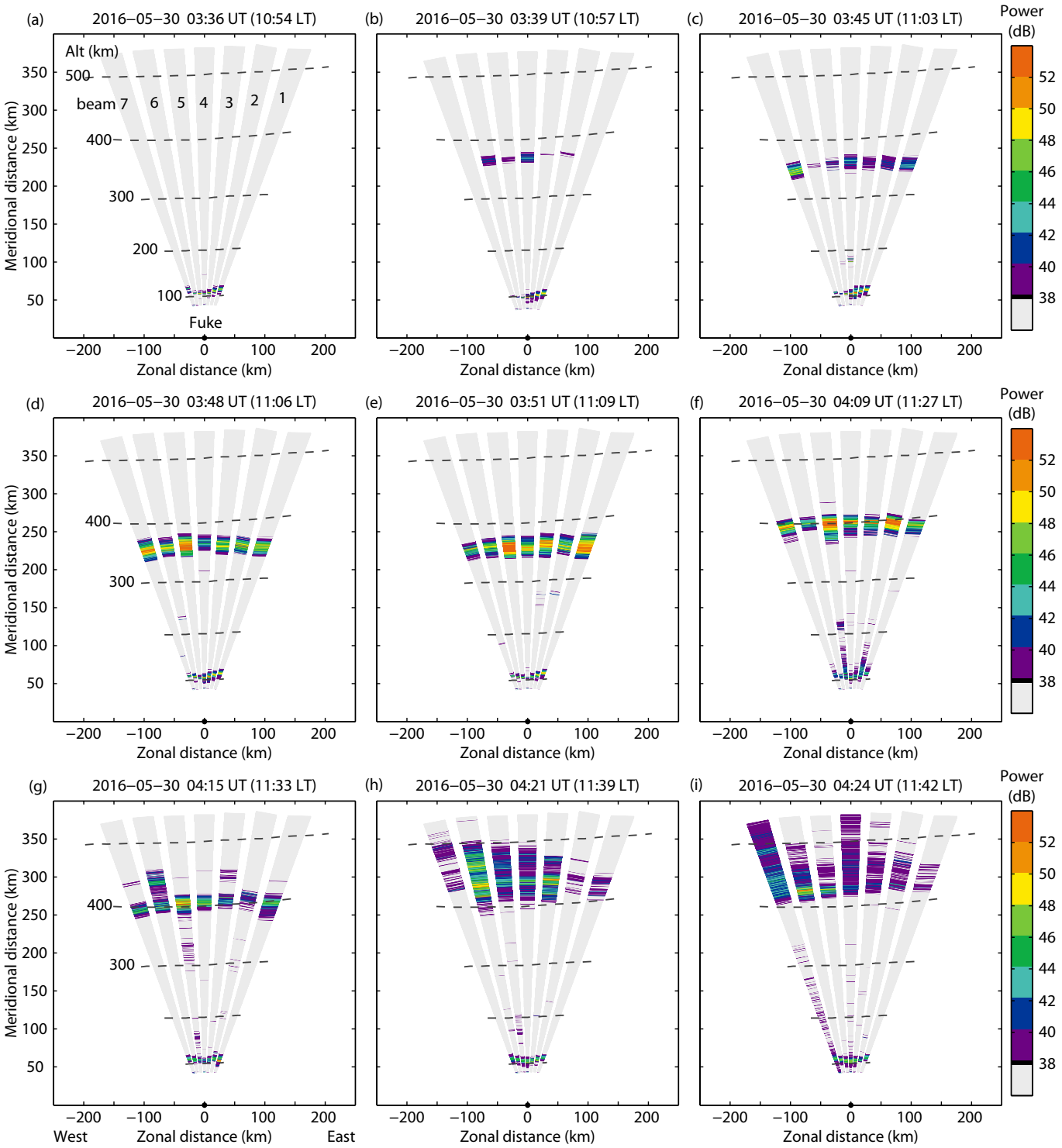

Figure 16. The fan sector maps of echo power (in dB) taken from 10:54 LT (03:36 UT) to 11:42 LT (04:24 UT) showing the onset and growth of F-region irregularities. After Li GZ et al. (2018a).

The strong amplitude scintillation occurs primarily at the azimuth angle of 180°–200°, and the LoL of GPS at azimuth of 170°–180° (Figure 17).

Xu L et al. (2019) proposed to use the standard deviation of the TEC fluctuation as a characteristic parameter serving as an indicator of the strength of the phase scintillation that would avoid the influence of the ionospheric projection of the satellite velocity and the ionospheric irregularity drift. This TEC fluctuation index is equivalent to the phase scintillation index, with the advantage of facilitating batch processing of large data without human intervention.

Wang GJ et al. (2019) reported global observations of the *S*4 amplitude scintillation index by the GPS Occultation Sounder (GNOS) on the Fengyun-3 C (FY3C) satellite. The observations reveal glob-

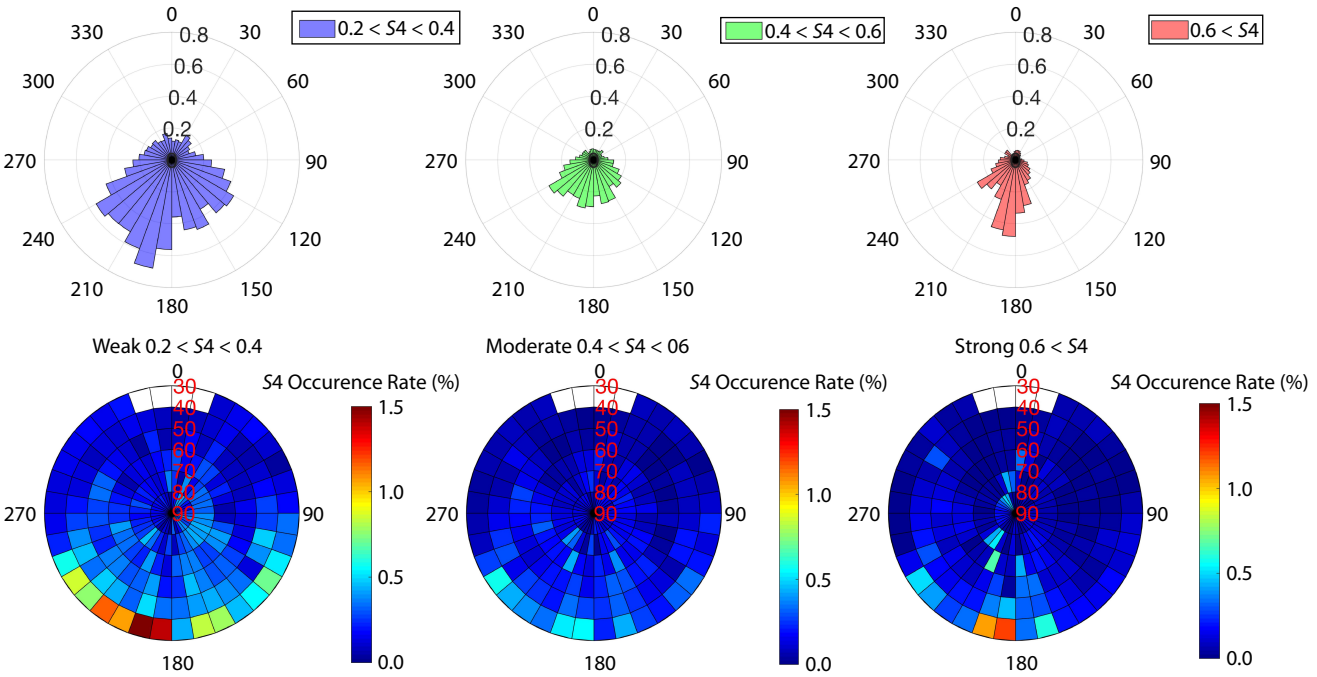

Figure 17. Spatial distribution of six years averaged amplitude scintillation occurrence in Shenzhen with different *S*4 intervals. After Zhang M et al. (2019).

al dynamic patterns of strong pre-midnight scintillations in the ionospheric F-region during the St. Patrick's Day geomagnetic super storm of 17–19 March 2015. During the main phase of the March 17 storm, the scintillations were first triggered at 160°E longitude in the New Zealand sector, extending beyond 40°S dip latitude. The scintillations were enhanced also in the Indian sector, but significantly suppressed in East Asia near 120°E longitude and in Africa around 30°E longitude. This pattern is consistent with the density depletion structures detected by the C/NOFS satellite and ground-based instruments.

Wang N et al. (2018) investigated the Spread-F at four ionosondes located at Haikou (20°N, 110.34°E), Guangzhou (23.14°N, 113.36°E), Beijing (40.11°N, 116.28°E), and Changchun (43.84°N, 125.28°E). The frequency Spread-F (FSF) occurrences show a negative correlation with solar activity at all four sites; range Spread-F (RSF) positive occurrence correlates with solar activity at Haikou. The frequency Spread-F appears more often after midnight with higher occurrence at mid-latitudes and summer months. The range Spread-F in 2000–2002 at HK and GZ occurred mostly in the equinoctial months. The favorable virtual height of the F layer for RSF occurrence ranged between 240 and 290 km.

Wang N et al. (2019a) and Wang N et al. (2019b) investigated the Spread-F and made comparative study of Spread-F and scintillation occurrence rates in East Asia. The occurrence of FSF is oppositely correlated with solar or geomagnetic activities. The occurrence of FSF is higher than that of RSF. The FSF occurs more frequently in summer; a higher RSF occurrence is seen in winter at latitude near 45°N. The Spread-F occurrence is higher in the coastal areas than in the continental region between 35°N and 45°N latitudes; no remarkable difference is observed at lower latitudes.

Liu Y et al. (2018c) investigated the statistical characteristics of global sporadic E (E_S) occurrence and its relation with wind shear by using GNSS radio occultation measurements and the TIMED/TIDI dataset from 2002–2016. They report that E_S occurrences had distinct temporal and spatial variations, which reached a maximum at local daytime and the post-sunset period in summer (winter) season in the Northern (Southern) hemisphere. The wind shear was found to play a significant role in the formation of E_S, especially in the mid-latitude region.

Zhou C et al. (2018a) showed the morphology of the E region field-aligned irregularity (FAI) at Wuhan by using 2015–2016 Wuhan VHF radar observations. Quasi-period echoes were observed frequently in summer post-sunset periods in the height range of 100–120 km. Doppler spectra reveal that the type 2 irregularity is dominant during the observational period. Wuhan ionosonde data from 2015–2016 revealed a strong linkage between E region FAI and E_S. Several mechanisms, such as Kelvin-Helmholtz instability (KHI) or ES instability, could be considered as the possible mechanism for the generation of E region FAI in the mid-latitude region.

By using Wuhan VHF radar, Wuhan GNSS network, and Wuhan ionosonde, Liu Y et al. (2019b) investigated mid- and low- latitude nighttime ionospheric E–F coupling. Results show that E- and F-region irregularities, nighttime MSTIDs, strong E_S, and Spread F were simultaneously observed on May 25, 2016. Our results provide the first observational evidence of the full electrodynamic links among different ionospheric irregularities in the mid- and low- latitude nighttime region of China.

Chen GY et al. (2019) investigated medium-scale traveling ionospheric disturbances (MSTIDs) by using the Hong Kong Continuously Operating Reference Stations network with a short baseline

length of 10–15 km. The occurrence rate of MSTIDs has a strong dependence on local time and season. They categorized the MSTIDs during 2014–2017 into three types. They observed no distinguishable difference in the MSTID parameters between the cyclone period and non-cyclone period.

Jiang CH et al. (2019a) carried out a modeling study of the F_2 layer stratification on ionograms using a ray tracing method based on a simple model of TIDs. Results show that gravity waves/TIDs might play a significant role in formation of the F_2 layer stratification. TIDs induced gradients could cause different features on ionograms. The F_2 layer stratification is due primarily to the vertical gradient in the ionosphere, and the horizontal gradient could lead to spread F on ionograms. Jiang CH et al. (2019b) further conducted a statistical study of the F_2 layer stratification at Puer station (22.7°N, 101.05°E, dip Lat. 12.9°N) in 2015 and 2016. The F_2 layer stratification occurs at daytime and nighttime, moving upward and downward. The new cusp could originate from different positions on ionograms. Statistical studies show that the daytime F_2 layer stratification occurred later in winter. The post-midnight F_2 layer stratification could be observed frequently on spring days.

Yang GB et al. (2018) studied daytime spread F at Zhangye station (39.4°N, 100.0°E, dip Lat. 29.6°N). The ionosonde recorded three incidences of daytime spread F on 6 January, 2017. The daytime spread F observed might be attributed to Traveling Ionospheric Disturbances (TIDs)/atmospheric gravity waves induced by a geomagnetic storm.

Spread F occurred frequently at Puer station. Lan T et al. (2018) developed a method for automatic identification of Spread F using decision trees. Lan T et al. (2019) further carried out a statistical study of Spread F detected at Puer station in the years of 2015 and 2016. FSF and MSF were dominant at Puer. Most types of SF appeared mostly in summer, and the maximum occurrence of SSF in equinox. They suggested that medium-scale traveling ionospheric disturbances (MSTIDs) may play a key role in formation of SF.

Zhou C et al. (2018b) investigated the coupling between ionosphere E and F regions at Wuhan by using Wuhan ionosonde and VHF coherent scatter radar, and Mengcheng airglow imager. Diffuse E_S layers and E region irregularities are related to F region medium-scale traveling ionospheric disturbances or spread F through polarized electric field mapping along the field lines. Wuhan ionosonde and VHF radar data from 2015 to 2016 show that the coincidence of diffuse E_S layers, E region FAIs, and spread F is much higher at nighttime. Their work indicates that polarized electric field generated in the E region irregularity could map to the F region and excite an electrodynamic process, such as Perkins instability, which would be important for nighttime midlatitude ionospheric E and F region coupling.

Meng X et al. (2019) reported band-like irregularity structures with a short lifetime. The structures appeared initially at altitudes higher than 400 km and moved to still higher altitudes but without zonal propagation. The band-like irregularities were accompanied by spread echoes.

Low frequency plasma instabilities are considered to be a dominant mechanism generating ionospheric irregularities. Laboratory experiments can provide an instructive approach to understanding ionospheric plasma instabilities, waves, and irregularities. Compared to a satellite mission or rocket campaign, laboratory experiments (Figure 18) have many advantages, such as reproducibility, controllability, diagonality, and reconfigurability. Liu Y et al. (2018a, b) designed and performed controlled experiments to simulate the ionospheric collisional plasma environment, providing evidences that the low frequency plasma instabilities such as the Kelvin–Helmholtz instability (KHI) can be generated in an ionospheric-like plasma. Through their experimental work, theoretical mechanisms can be more confidently applied to explain the excitation of ionospheric irregularities.

5. Modeling and Data Assimilation

Aa et al. (2018b) presented a data ingestion technique to incorporate Madrigal TEC data into the NeQuick 2 model. Their method is based on retrieving an appropriate global distribution of the

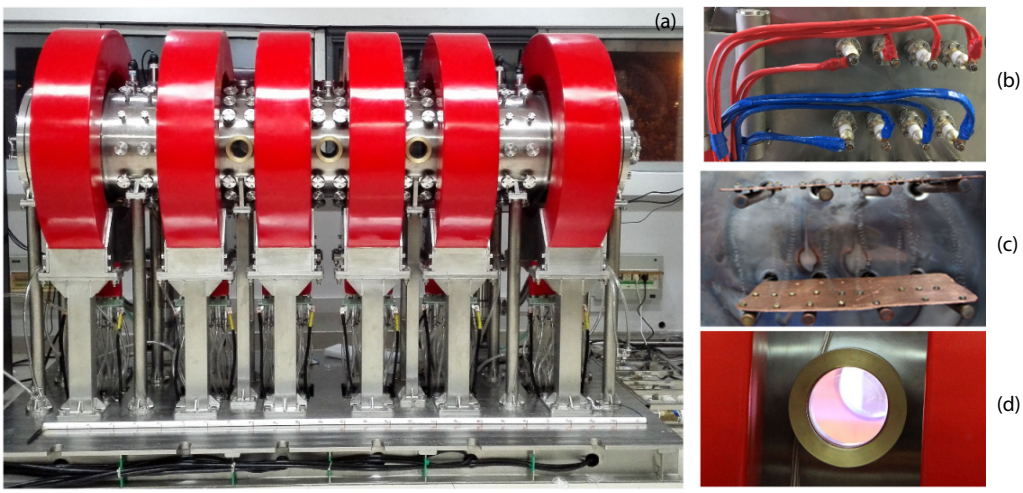

Figure 18. (a) Front view of the Keda Space Plasma EXperiment (KSPEX), (b) the Kovar electrodes used for heating filaments, (c) arrangement of the filaments in the primary chamber, and (d) a picture of the double layer plasmas. Picture is provided by Liu Y. (private communication).

effective ionization parameter (A_z), which can be implemented through minimizing the difference between the measured and modeled TEC at each grid in local time-modified dip latitude coordinates. The NeQuick 2 model could be driven by an A_z map to reproduce ionospheric parameters, such as N_e, TEC, N_mF_2, h_mF_2, and so forth. Their validations show that a general improvement in accuracy of 30%–50% can be achieved after data ingestion. In addition, the empirical orthogonal function (EOF) analysis technique is used to construct a parameterized time-varying global A_z model. The NeQuick TEC driven by EOF-modeled A_z shows 10%–15% improvement in accuracy over the standard ionosphere correction algorithm in the Galileo navigation system.

The global ground based GNSS slant TEC is widely used as the source of ionospheric data for assimilation. Given that more ground GNSS receivers have the capability to track multiple navigation signals, She CL et al. (2020) proposed a new method to estimate the receiver's differential code bias (DCB), based on the assumption that the ionosphere has local spherical symmetry; this assumption allows calibration of the slant TEC self-consistently without the aid of another data source or model. He JH et al. (2019) constructed an ensemble Kalman filter (EnKF) ionosphere and thermosphere data assimilation system using the National Center for Atmospheric Research Thermosphere Ionosphere Electrodynamics General Circulation Model (NCAR-TIEGCM) as the background model. They use a sparse matrix method to avoid significant matrix related calculation and storage. A series of observing system simulation experiments have been conducted to assess the performance of the system. The results show that the system optimizes ionosphere drivers efficiently by assimilating electron densities through their covariance. The short-term forecast capability is enhanced significantly, and the effect of initial condition correction lasts for longer than 24 h. Their study demonstrates that EnKF based global ionosphere and thermosphere data assimilation can be conducted without using a supercomputer. Their ionosphere and thermosphere data assimilation system benefits both scientific studies and near real-time operation.

Liu ZD et al. (2019) performed a validation of the predictions of the IRI-2016 model by using ionosonde measurements from 4 Chinese stations. They found that the daily minimum value of f_oF_2 occurs earlier in the IRI-2016 prediction than in the observations. Around sunrise, the IRI-2016 prediction shows a very sharp rise, much faster than the observed f_oF_2. The CCIR option of IRI is found to perform better than the URSI option during postsunset under low solar activity or in the EIA region over China.

Wang SC et al. (2018) developed a dual-parameter regularization algorithm to reconstruct the three-dimensional ionospheric electron density under the assumption that ionospheric spatial variations can be separable into the horizontal and vertical directions. Wang SC et al. (2019) adopted the Tikhonov regularization method to reconstruct the 3-D ionospheric electron density by incorporating electron density profiles data from COSMIC radio occultation technique and ground ionosondes. A regularization parameter was introduced to balance the weights between prior (or background) information and new measurements. The model function in the modified *L*-curve method is used to determine the optimal regularization parameter.

Zhao XR et al. (2019) developed an algorithm to determine the wave turbopause based on numerical differentiation. Tikhonov regularization is used to solve reasonably the ill-posed numerical differential problem, which laid a foundation for determining quantitatively the wave turbopause in the lower ionosphere by using the vertical gradient profile of the temperature standard deviation.

6. Radio Wave Propagation in the Ionosphere and Sounding Techniques

For many years a number of ionosondes have been operated in China to detect ionospheric disturbances. The ionosondes, however, are not very suitable for short-period (<15 minutes) disturbances, due to their limited time resolutions (>5 min). In recent years the Institute of Geology and Geophysics, Chinese Academy of Sciences, together with the South Central University for Nationalities, has been developing a portable digital ionosonde (PDI) equipped with improved capability to detect and characterize small-scale/short-period ionospheric disturbances; the PDI can be assembled quickly and set up at temporary field stations for campaign coordinated observations. Lan JP et al. (2018) performed a preliminary analysis of observations employing a PDI at Sanya (18.3°N, 109.6°E). Their results show the presence of ionospheric disturbances with periods ranging from several to tens of minutes. Interestingly, the disturbances (with different periods) were found to occur simultaneously at different F region altitudes, for example, with periods of ~5 and 20 minutes below and above ~180 km, respectively (Figure 19). The absence of shorter-period disturbance at higher altitudes is consistent with the fact of acoustic gravity waves through the region with intrinsic periods above the Brunt–Väisälä period. Their results demonstrate the capability of PDI in routine ionogram mode to detect ionospheric disturbances with temporal scales down to a few minutes.

An ionogram captures important ionospheric information. For real-time monitoring of the ionosphere it is essential to achieve automatic scaling and inversion of ionograms with accuracy as high as possible. Chen ZW et al. (2018) developed such a method to scale ionograms automatically, based on pattern recognition technology, mathematical morphology, and the echo characteristics of each layer of the ionosphere. The method has low computational complexity, strong universality, and high accuracy (over 90%) when it was used to scale observations of Chinese Academy of Sciences Digital Ionosonde (CAS-DIS). The method can deal with ionograms in routine situations and also when ionograms exhibit irregularities.

An Ionospheric Observation Network for Irregularity and Scintillation in East/Southeast Asia (IONISE, http://ionise.geophys.ac.cn/) was recently deployed by Beijing National Observatory of Space Environment (Figure 20). Using ionospheric total electron content (TEC) data from the two crossed Beidou geostationary satellite receiver chains of the network along 110°E and 23°N, and Doppler velocity measurements from the Sanya (18.3°N, 109.6°E) portable digital ionosonde, Li GZ et al. (2019) reported observations of low

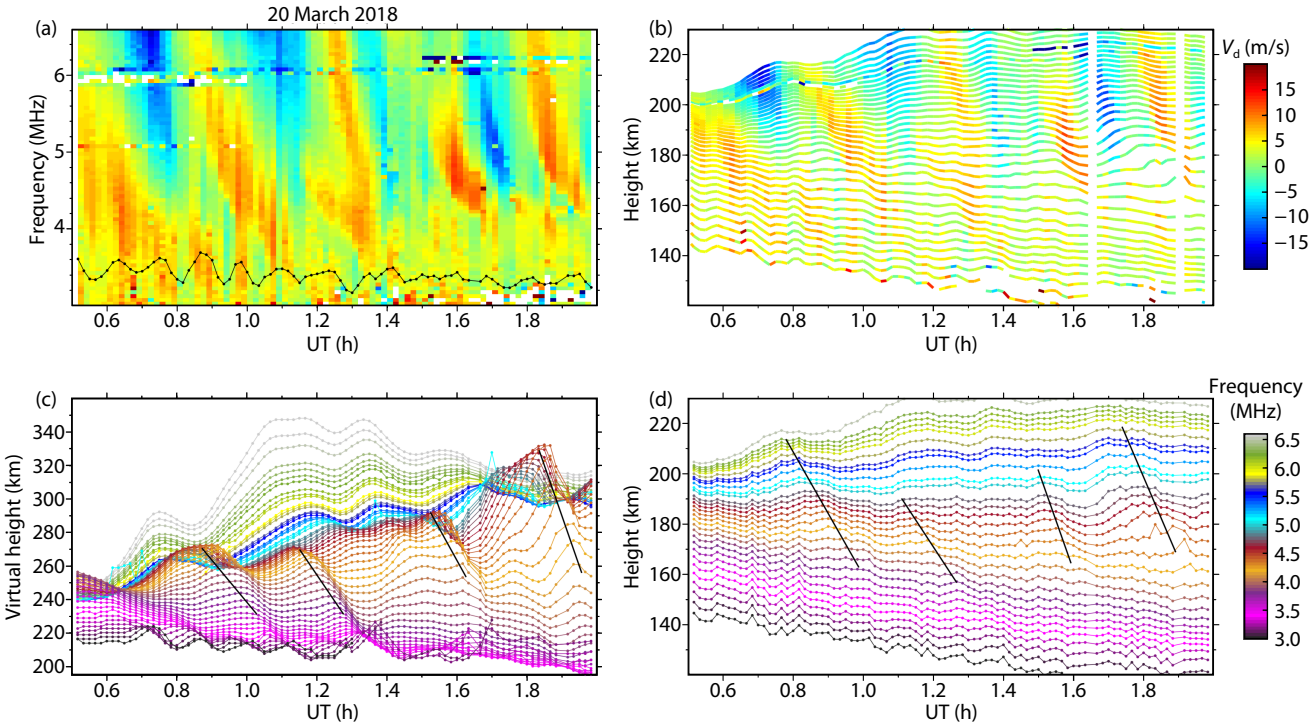

Figure 19. Doppler velocity as functions of (a) sounding frequency and time, and (b) true height and time, and temporal variations of (c) virtual height and (d) true height for the plasma frequencies of 3–11 MHz indicated by different colors during 00:30–02:00 UT on 20 March 2018. After Lan JP et al. 2018.

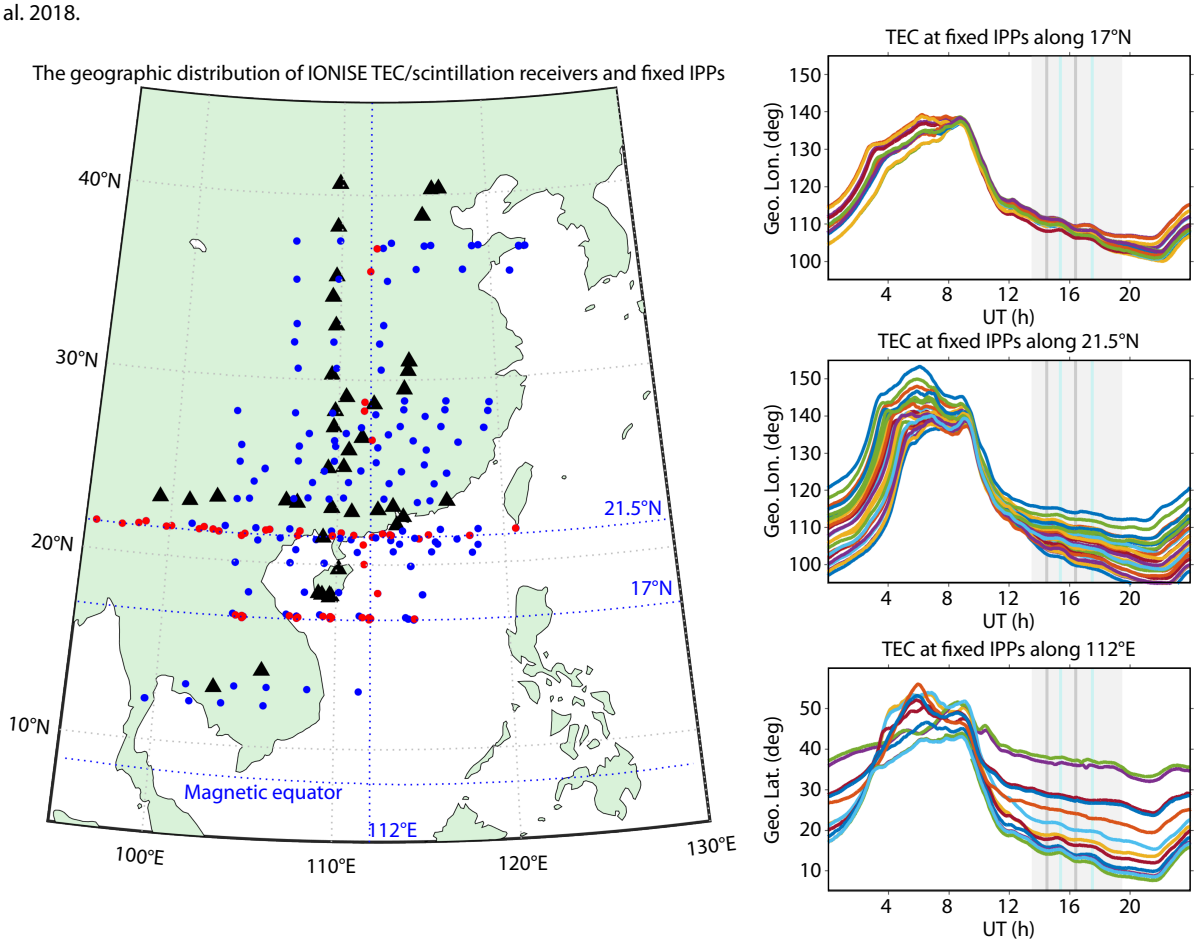

Figure 20. Map of the IONISE TEC/scintillation receivers (marked with triangles) and fixed ionospheric pierce points (marked with dots) (after Li GZ et al., 2019). For the near real-time IONISE plots please visit http://ionise.geophys.ac.cn/. Samples of TEC are also given in the right panels.

latitude TEC oscillations synchronized over a wide longitude range in East/Southeast Asia, which occur at nighttime, after the main phase of the 20 April 2018 geomagnetic storm. Their results show that the periodic TEC enhancements correlate with F region downward plasma drifts and IMF B_z southward turnings. They suggest that the quasiperiodic southward turnings of IMF B_z could produce multiple short-lived westward prompt penetration electric fields, which contribute to drive the nighttime low latitude TEC oscillations simultaneously over the wide longitude range. Compared with TEC measurements by GPS receiver networks that are affected by satellite motion, the IONISE, which measures TEC at fixed ionospheric pierce points along the same longitude/latitude by receiving Beidou geostationary satellite signals, provides a unique means for fine-scale observations of ionospheric perturbations.

The Chinese Beidou Navigation Satellite System (BDS) now provides an excellent opportunity to facilitate investigation of ionospheric structures. Huang FQ et al. (2018) used the Beidou GEO TEC to detect characteristics of nighttime medium-scale traveling ionospheric disturbances (MSTIDs) at middle latitudes, and compared them with those from airglow images and GPS TEC observations. In data from 2016, three peaks were found in the seasonal variations of the nighttime MSTID occurrence rate. Moreover, features of nighttime MSTIDs detected in data from the Beidou GEO TEC are found to be in better agreement with those from airglow images than those from the GPS TEC, given that the GPS TEC results are affected by Doppler shift and ionospheric background TEC due to movement of GPS satellites. Huang FQ et al. (2019) first analyzed daytime ionospheric periodic wave-like structures in the low-latitude ionosphere over the Asian-Australian sector using TEC from Beidou GEO observations. They found that these structures have periods of about 18–28 minutes and show obvious seasonal, LT, and latitudinal variations. No clear correlation between the two Hemispheres is found. They argue that daytime ionospheric periodic wave-like structures in the low-latitude ionosphere could be triggered by GWs from the lower atmosphere, and generated in the low-latitude ionosphere rather than propagating from other latitudes.

Zhao JQ and Zhou C (2018) proposed the concept of optimal ionospheric shell height to minimize the absolute values of DCB. Based on data from five IGS stations at different latitudes during 2003–2013, their results show that the optimal ionospheric shell height performs much better than the fixed ionospheric shell height. The optimal ionospheric shell heights show 11-year and 1-year periods and latitudinal dependence.

Zhao JQ and Zhou C (2019) examined whether the optimal ionospheric shell height derived from IGS stations can be applied to non-IGS stations or isolated GNSS receivers. Their study shows that the optimal ionospheric shell height calculated by reference IGS stations can be applied to its nearby non-IGS stations or isolated GNSS receivers for accurate TEC estimation, and that the error of DCB estimation by a nearby non-IGS station or isolated GNSS receiver is generally linear with the distance from the reference IGS station.

The existence of GNSS differential code biases (DCBs) provides a challenge for estimating the ionospheric TEC. Li M et al. (2018) comprehensively assessed the intra-day stability of receiver DCBs over a period of 1 month in terms of hour-to-hour estimating of multi-GNSS receiver DCBs. Their extracted receiver DCBs may not change abruptly in two consecutive days, but instead shift gradually over short-term intervals. They also verified that when significant short-term variations occur in the derived receiver DCBs, the assumption of constant receiver DCBs will partially account for the observed errors in ionospheric TEC extraction (with the RMS of 12.96 TECu).

Dual-frequency GNSS receivers are widely used for sensing the earth's ionosphere. Zhao CH et al. (2019) proposed a multi-GNSS single-frequency (MSF) precise point positioning approach that would enable simultaneous retrieval of VTEC with low-cost MSF receivers. The ionospheric VTEC estimated using their MSF approach reaches the same level of accuracy as that of the dual-frequency approach.

The ionospheric E_S layer has significant impact on radio wave propagation. The traditional techniques employed for E_S layer observation — for example, ionosondes — are not dense enough to resolve the morphology and dynamics of the E_S layer in spatial distribution. Based on the Chinese ground-based GNSS networks, including the Crustal Movement Observation Network of China and the Beidou Ionospheric Observation Network, Sun WJ et al. (2019) observed a large-scale strong E_S event in the middle latitude of China. The strong E_S, shown as a band-like structure in the southwest-northeast direction, extended more than 1,000 km. By making a comparative analysis of E_S occurrences identified statistically from simultaneous observations by ionosondes and GNSS TEC receivers over China's middle latitude, they found that GNSS TEC can be well employed to observe strong Es occurrences with a threshold value of f_oE_S.

Using total electron content (TEC) data from 902 global navigation satellite system stations over China, Liu HT et al. (2018) analyzed ionospheric responses following two similar launches of the Long March 4B from Taiyuan, China — that is, the China–Brazil Earth Resources Satellite 3 launched on 9 December 2013 and the China–Brazil Earth Resources Satellite 4 launched on 7 December 2014. The ionospheric disturbances of these two launches were found to be almost the same; three types of disturbances were observed following both launches: depletions, shock wave-related traveling ionospheric disturbances (TIDs), and acoustic wave-related circle TIDs. The buildup time of depletion was influenced by the amount of exhaust expelled into the ionosphere. After the electron depletion was formed, it drifted westward for approximately 300 km. The shock wave-related TIDs could be observed only near the trajectory and reflected the acceleration of the rockets. The acoustic wave-related circle TIDs were observed at the southeast of the launch site.

The rapidly developing GNSS constellations give us unprecedented abilities to monitor and study the near-Earth space. Hao YQ et al. (2018) recently used GNSS beacons to investigate the prompt response of the plasmasphere to an interplanetary shock. Data from the Beidou Navigation Satellite System and GPS receivers were used to examine sudden TEC variations when the shock im-

pinged on the dayside magnetosphere on March 17, 2015. The dense GNSS constellations and globally distributed ground receivers may enable us to estimate the propagation velocity of a shock-induced pulse in the magnetosphere.

Ding ZH et al. (2018a) introduced the configuration and implementation of the Qujing incoherent scatter radar (QJISR), including its antenna, transmitter, receiver, signal processing, and data analysis. They reported some preliminary observations of the raw echoes and power spectra, and the derived ionospheric parameters (electron density, electron temperature, and ion temperature).

Wu J et al. (2018) reported a remarkable extension of observing altitudes of the high frequency pumping enhanced plasma line (HFPL) and the ion line (HFIL) in the observations of the ultrahigh frequency incoherent scatter radar (UHF-ISR) of the European Incoherent Scatter scientific association (EISCAT), implying that the enhanced ion acoustic wave and Langmuir wave should satisfy the Bragg condition within the extended altitude range. The dependence of the wave-number of the traveling ion acoustic wave on the profile of enhanced electron temperature and ion mass leads to extension of observing altitudes of the enhanced ion line; the extension is dependent on the profile of the electron density, the enhanced electron temperature, and the thermal conduction along the magnetic field.

Wu J et al. (2019) further reported that the enhanced electron temperature plays a significant role in determining the intensities of the enhanced Langmuir and ion acoustic waves by the parametric decay instability and the oscillation two-stream instability. The intensities of the enhanced plasma and ion lines depend on the Bragg condition's being satisfied by the enhanced Langmuir and ion acoustic waves. The overshoots in the enhanced plasma and ion lines may be attributed to anomalous absorption of the pump and modifications of the plasma on the propagating path of the enhanced Langmuir and ion acoustic waves.

Lv LB et al. (2018) derived the scattering equations of electron density fluctuations generated by HF heating based on the scattering theory of anisotropic irregularities, with assumptions of a Gaussian autocorrelation function. The variances of scattering coefficients with the geomagnetic field, effective radiated power (ERP), and frequency were studied by numerical simulations. The scattering coefficients are larger at high latitudes than at mid and low latitudes under the same conditions. According to the simulations, the scattering coefficients with an HF pumping ERP exceeding 250 MW at Wuhan or 650 MW at Guangzhou can have magnitude comparable with those at Platteville to support VHF transmission on long-distance circuits.

Xu T et al. (2019) performed a polarization analysis of beat-wave (BW) — generated extremely low frequency (ELF)/very low frequency (VLF) waves using the EISCAT heating facility near Tromsø. The ELF/VLF waves can be decomposed into right-(R) and left-(L) handed circularly polarized waves with comparable strengths, and the polarization ellipse tends to be parallel to the well-known dominant background electric field, consistent with recognized features of ELF/VLF waves generated by PEJ modulation. Hence, their result demonstrates that the BW-generated current is located in the D/E region, not in the F region.

Yang JT et al. (2018a) examined the effect of the duty cycle and heating frequency on the radiation efficiency of VLF/ELF in amplitude modulated ionospheric heating experiments by using simulations of the lower-ionosphere modulated heating model. The numerical simulation shows that the intensity of the VLF/ELF equivalent radiation changes from increase to decrease with increasing modulated duty cycle and heating frequency.

Yang JT et al. (2018b) investigated modulated ionospheric heating by using the EISCAT facility in Tromso, Norway. The experiments show that, in the amplitude modulated (AM) mode, the amplitude of the ELF/VLF signal has a peak at 2017 Hz. In the beat-wave (BW) mode, the maximum appears at 2017 Hz, but the overall amplitude of the ELF/VLF signal increases with the radiation frequency. When the frequency is low, the ELF/VLF signal that is excited has larger amplitude in the AM mode than in the BW mode. In contrast, the BW mode performs better than the AM mode at higher frequency. The AM mode tends to produce circularly polarized waves, and the BW mode produces linearly polarized waves.

Yang JT et al. (2019) reported experiments of ELF/VLF radiation from the ionosphere by AM mode and dual-beam beat-wave (BW) mode modulation heating using the EISCAT heating facility. In the AM mode, the intensity of the ELF/VLF radiation source depends on the intensity of the geomagnetic disturbance and on the magnitude of natural currents in the ionosphere. In the BW mode, the intensity of the ELF/VLF radiation source is less dependent on the intensity of the geomagnetic disturbance.

Yu TT et al. (2019) constructed an empirical model of GUVI neutral density aiming to solve the difficulty of direct comparison of GUVI and CHAMP observations due to their different local times at a given location on a given day. The GUVI model is in good agreement with CHAMP observations, with small standard deviations of their ratios (less than 10%) except at low solar flux levels. The correlation coefficients are greater than 0.9, and the relative standard errors are less than 20%. Comparison between the GUVI model and CHAMP observations during solar minimum shows a large bias (~30%). Their results demonstrate the validity and accuracy of the model based on GUVI data against the density data from the CHAMP satellite.

Meteoroids entering the Earth's atmosphere can create meteor trail irregularity, seriously disturbing the background ionosphere. By installing multiple video cameras near the Sanya VHF radar site, Li GZ et al. (2018b) conducted an observational campaign during the period from November 2016 to February 2017. Their results show good agreement between the angular positions of non-specular echoes and those of optical meteors, which verify the interferometry capability of Sanya radar for meteor trail irregularity observation. The non-specular echo duration was found to have a generally linear relationship with its corresponding meteor visual magnitude. Furthermore, in some cases optical meteors were detected, while there are no simultaneous radar non-specular echoes, indicating that some optical meteors may appear at extremely low altitudes.

Bai WH et al. (2019) compared ground-based ionosonde observations with GNSS occultation sounder (GNOS) results from a radio

occultation sounding payload onboard the Fengyun 3 C (FY3-C) satellite. They verified the reliability of results of radio occultation data from an event investigation of the March 2015 magnetic storm, and a correlation analysis between ionosonde data and peak electron densities (N_mF_2) derived from GNOS Global Position System (GPS) and Beidou navigation system (BDS) data.

Sui Y et al. (2019) investigated ionospheric effects on phase and Faraday rotation of interferometry for the TwinSAR-L synthetic aperture radar SAR mission (Terrain Wide-swath Interferometric *L*-band mission) for global earth remote sensing, which will be launched by China in the future.

Fu HY et al. (2018a) investigated the asymmetry in stimulated emission polarization and irregularity evolution during ionospheric electron gyroharmonic heating. High-frequency radar echoes and stimulated electromagnetic emission (SEE) polarimetry appear asymmetric for pumping above $3f_{ce}$ (f_{ce}, the electron cyclotron frequency), implying that the broad upshifted maximum spectral line formation involves plasma irregularities scattered by high-frequency radar echoes. Fu HY and Scales (2018) established a two-dimensional kinetic model of stimulated electromagnetic emissions to investigate this SEE asymmetry near the electron gyro harmonic.

Incoherent scatter radar (ISR) is the most powerful ground-based measurement method for studying the ionosphere. Plasma lines are not routinely detected by ISR, usually falling below the measured spectral noise level; however, they are occasionally enhanced by suprathermal electrons through the Landau damping process and become detectable by ISR. Wang X and Zhou C (2018) derived the electron density from plasma lines induced by suprathermal electron in an ionospheric modification experiment. The European Incoherent Scatter Association (EISCAT) UHF incoherent scatter radar observed the enhanced plasma lines, considering as a manifestation of the suprathermal electrons generated by the high-frequency heating wave during the ionospheric modification experiment.

Wang X. et al. (2018a) conducted a theoretical investigation of the threshold of parametric instability in ionospheric heating experiments. A general dispersion relation and the threshold of the parametric instability excitation in the heating experiment are derived by considering the inhomogeneous spatial distribution of that pump wave field. They showed that the threshold of parametric instability is influenced by the effective electron and ion collision frequencies and the pump wave frequency. Both collision and Landau damping should be considered in the parametric instability calculation.

Wang X et al. (2018b) investigated the generation of small-scale field aligned irregularities in ionosphere heating experiments, using a theoretical model to describe small-scale irregularities excited by powerful high frequency (3–30 MHz) electromagnetic waves. The model is based on the transport equation in magnetic plasma and mode conversion from electromagnetic wave to electrostatic wave in ionospheric modification. The calculations indicate that background electron density and geomagnetic field play an important role in determining the threshold electric field and the spatial scale of the electron density irregularities. The electric field threshold is found to increase with decreasing spatial scale of the irregularities.

Wang X et al. (2019) investigated the stimulated electromagnetic emissions (SEEs) spectrum observed during an X-mode heating experiment at the EISCAT (European Incoherent Scatter Scientific Association). SEEs spectra were observed from the EISCAT high-power high-frequency transmitter facility located at Tromsø. A narrow continuum occurred under cold-start conditions and showed an overshoot effect lasting several seconds. Cascading peaks occurred on both sides of the heating frequency only in the preconditioned ionosphere, also showing an overshoot effect.

Liu MR et al. (2018) investigated ionospheric heating by oblique incidence of powerful HF radio waves using three-dimensional numerical simulations. They established a model to simulate three-dimensional ionospheric heating by oblique incidence of powerful HF radio waves. A plane wave spectral integral method is used to calculate the electric field in the caustic region. The simulation results indicate that the ionospheric electron density and temperature can be disturbed by oblique incidence of powerful radio waves, especially in the caustic region. They compared the effects of heating with waves incident in the parallel and perpendicular directions to the geomagnetic field. The ionospheric modulation is found to be more effective when the heating wave propagates longitudinally.

Acknowledgments

Libo Liu would like to express his gratitude to colleagues for kindly providing their articles and pictures in the course of the preparation of this national report. The contributors are Aa E., Gang Chen, Yiding Chen, Ziwei Chen, Tong Dang, Feng Ding, Zonghua Ding, Hanxian Fang, Haiyang Fu, Yongqiang Hao, Fuqing Huang, He Huang, Xingliang Huo, Huijun Le, Jiuhou Lei, Guozhu Li, Guoqi Liu, Y.-Y. Sun, Hui Wang, Zheng Wang, Yewen Wu, Xiangxiang Yan, Na Yang, Tao Yu, Xinan Yue, Beichen Zhang, Dengke Zhang, Donghe Zhang, Qinghe Zhang, Ruilong Zhang, Biqiang Zhao, Chen Zhou, Zhenping Zhu. This report was financially supported by National Natural Science Foundation of China (41774161, 41621063) and by the Open Research Project of Large Research Infrastructures of CAS — "Study of the interaction between low/mid-latitude atmosphere and ionosphere based on the Chinese Meridian Project".

References

Aa, E., Huang, W. G., Liu, S. Q., Ridley, A., Zou, S. S., Shi, L. Q., Chen, Y. H., Shen, H., Yuan, T. J., … Wang, T. (2018a). Midlatitude plasma bubbles over China and adjacent areas during a magnetic storm on 8 September 2017. *Space Wea.*, *16*(3), 321–331. https://doi.org/10.1002/2017SW001776

Aa, E., Ridley, A. J., Huang, W. G., Zou, S. S., Liu, S. Q., Coster, A. J., and Zhang, S. R. (2018b). An ionosphere specification technique based on data ingestion algorithm and empirical orthogonal function analysis method. *Space Wea.*, *16*(9), 1410–1423. https://doi.org/10.1029/2018SW001987

Aa, E., Zou, S. S., Ridley, A. J., Zhang, S. R., Coster, A. J., Erickson, P. J., Liu, S. Q., and Ren, J. E. (2019). Merging of storm time midlatitude traveling ionospheric disturbances and equatorial plasma bubbles. *Space Wea.*, *17*(2), 285–298. https://doi.org/10.1029/2018SW002101

Aa, E., Zou, S. S., Eastes, R., Karan, D. K., Zhang, S. R., Erickson, P. J., and Coster, A. J. (2020). Coordinated ground-based and space-based observations of equatorial plasma bubbles. *J. Geophys. Res.: Space Phys.*, *125*(1),

e2019JA027569. https://doi.org/10.1029/2019JA027569

Bai, W. H., Wang, G. J., Sun, Y. Q., Shi, J. K., Yang, G. L., Meng, X. G., Wang, D. W., Du, Q. F., Wang, X. Y., … Liu, C. (2019). Application of the Fengyun 3 C GNSS occultation sounder for assessing the global ionospheric response to a magnetic storm event. *Atmos. Meas. Tech.*, *12*(3), 1483–1493. https://doi.org/10.5194/amt-12-1483-2019

Balan, N., Zhang, Q. H., Shiokawa, K., Skoug, R., Xing, Z. Y., Tulasi Ram, S., and Otsuka, Y. (2019). IpsDst of Dst storms applied to ionosphere–thermosphere storms and low-latitude aurora. *J. Geophys. Res.*: *Space Phys.*, *124*(11), 9552–9565. https://doi.org/10.1029/2019JA027080

Cai, Y. H., Yue, X. A., Wang, W. B., Zhang, S. R., Liu, L. B., Liu, H. X., and Wan, W. X. (2019). Long-term trend of topside ionospheric electron density derived from DMSP data during 1995–2017. *J. Geophys. Res.*: *Space Phys.*, *124*(12), 10708–10727. https://doi.org/10.1029/2019JA027522

Chen, G., Wang, J., Zhang, S. D., Deng, Z. X., Zhong, D. K., Wu, C., Jin, H., and Li, Y. X. (2018). Opposite latitudinal dependence of the premidnight and postmidnight oscillations in the electron density of midlatitude F layer. *J. Geophys. Res.*: *Space Phys.*, *123*(1), 796–807. https://doi.org/10.1002/2017JA024162

Chen, G. Y., Zhou, C., Liu, Y., Zhao, J. Q., Tang, Q., Wang, X., and Zhao, Z. Y. (2019). A statistical analysis of medium-scale traveling ionospheric disturbances during 2014–2017 using the Hong Kong CORS network. *Earth, Planets Space*, *71*, 52. https://doi.org/10.1186/s40623-019-1031-9

Chen, J. J., and Lei, J. H. (2019). A simulation study on the latitudinal variations of ionospheric zonal electric fields under geomagnetically quiet conditions. *J. Geophys. Res.*: *Space Phys.*, *124*(2), 1444–1453. https://doi.org/10.1029/2018JA026174

Chen, T., Wan, W., Xiong, J., Yu, Y., Ren, Z., and Yue, X. (2019). A statistical approach to quantify atmospheric contributions to the ITEC WN4 structure over low latitudes. *J. Geophys. Res.*: *Space Phys.*, *124*(3), 2178–2197. https://doi.org/10.1029/2018JA026090

Chen, Y. D., Liu, L. B., Le, H. J., and Wan, W. X. (2018). Responses of solar irradiance and the ionosphere to an intense activity region. *J. Geophys. Res.*: *Space Phys.*, *123*(3), 2116–2126. https://doi.org/10.1002/2017JA024765

Chen, Y. D., Liu, L. B., Le, H. J., and Zhang, H. (2019). Interhemispheric conjugate effect in longitude variations of mid-latitude ion density. *J. Space Wea. Space Climate*, *9*, A40. https://doi.org/10.1051/swsc/2019039

Chen, Z. W., Gong, Z. Q., Zhang, F., and Fang, G. Y. (2018). A new ionogram automatic scaling method. *Radio Sci.*, *53*(9), 1149–1164. https://doi.org/10.1029/2018RS006574

Dang, T., Lei, J. H., Wang, W. B., Zhang, B. Z., Burns, A., Le, H. J., Wu, Q., Ruan, H. B., Dou, X. K., and Wan W. X. (2018a). Global responses of the coupled thermosphere and ionosphere system to the August 2017 great American solar eclipse. *J. Geophys. Res.*: *Space Phys.*, *123*(8), 7040–7050. https://doi.org/10.1029/2018JA025566

Dang, T., Lei, J. H., Wang, W. B., Burns, A., Zhang, B. Z., and Zhang, S. R. (2018b). Suppression of the polar tongue of ionization during the 21 August 2017 solar eclipse. *Geophys. Res. Lett.*, *45*(7), 2918–2925. https://doi.org/10.1002/2018GL077328

Dang, T., Zhang, B. Z., Wiltberge, M., Wang, W. B., Varney, R., Dou, X. K., Wan, W. X., and Lei, J. H. (2018c). On the relation between soft electron precipitations in the cusp region and solar wind coupling functions. *J. Geophys. Res.*: *Space Phys.*, *123*(1), 211–226. https://doi.org/10.1002/2017JA024379

Dang, T., Lei, J. H., Wang, W. B., Wang, B. Y., Zhang, B. Z., Liu, J., Burns, A., and Nishimura, Y. (2019). Formation of double tongues of ionization during the 17 March 2013 geomagnetic storm. *J. Geophys. Res.*: *Space Phys.*, *124*(12), 10619–10630. https://doi.org/10.1029/2019JA027268

Ding, Z. H., Dai, L. D., Yang, S., Xu, Z. W., and Wu, J. (2018b). Preliminary measurement and analysis of the power spectra by the Qujing incoherent scatter radar. *Prog. Geophys.* (*in Chinese*), *33*(6), 2204–2210. https://doi.org/10.6038/pg2018BB0568

Ding, Z. H., Wu, J., Xu, B., Xu, Z. W., and Dai, L. D. (2018a). The Qujing incoherent scatter radar: system description and preliminary measurements. *Earth, Planets Space*, *70*, 87. https://doi.org/10.1186/s40623-018-0859-8

Ding, Z. H., Dai, L. D., Yang, S., et al. (2020). Preliminary analysis of the ionospheric electron temperature variations of F layer in daytime using the Qujing incoherent scatter radar measurements. *Chinese J. Geophys.* (*in Chinese*), *63*(4), 1282–1293.

Fu, H. Y., Scales, W. A., Bernhardt, P. A., Jin, Y. Q., and Briczinski, S. J. (2018). Asymmetry in stimulated emission polarization and irregularity evolution during ionospheric electron gyroharmonic heating. *Geophys. Res. Lett.*, *45*(18), 9363–9371. https://doi.org/10.1029/2018GL078957

Fu, H. Y., and Scales, W. A. (2018). Kinetic modeling of stimulated electromagnetic emissions during ionospheric heating experiment. In *12th International Symposium on Antennas, Propagation and EM Theory (ISAPE)*. Hangzhou: IEEE. http://doi.org/ 10.1109/ISAPE.2018.8634190

Guo, D. J., Lei, J. H., Ridley, A., and Ren, D. X. (2019). Low-density cell of the thermosphere at high latitudes revisited. *J. Geophys. Res.*: *Space Phys.*, *124*(1), 521–533. https://doi.org/10.1029/2018JA025770

Hao, Y. Q., Li, Q. H., Zhang, D. H., Xiao, Z., Yang, G. L., and Huang, C. (2018). Using GNSS TEC technique to observe compression of the plasmasphere by an interplanetary shock. *Sci. Sin. Technol.* (*in Chinese*), *48*(8), 853–862. https://doi.org/10.1360/N092017-00348

He, J. H., Yue, X. A., Wang, W. B., and Wan, W. X. (2019). EnKF ionosphere and thermosphere data assimilation algorithm through a sparse matrix method. *J. Geophys. Res.*: *Space Phys.*, *124*(8), 7356–7365. https://doi.org/10.1029/2019JA026554

Huang, F. Q., Lei, J. H., Dou, X. K., Luan, X. L., and Zhong, J. H. (2018). Nighttime medium-scale traveling ionospheric disturbances from airglow imager and Global Navigation Satellite Systems observations. *Geophys. Res. Lett.*, *45*(1), 31–38. https://doi.org/10.1002/2017GL076408

Huang, F. Q., Otsuka, Y., Lei, J. H., Luan, X. L., Dou, X. K., and Li, G. Z. (2019). Daytime periodic wave-like structures in the ionosphere observed at low latitudes over the Asian-Australian sector using total electron content from Beidou geostationary satellites. *J. Geophys. Res.*: *Space Phys.*, *124*(3), 2312–2322. https://doi.org/10.1029/2018JA026443

Huang, H., Lu, X., Liu, L. B., Wang, W. B., and Li, Q. L. (2018). Transition of interhemispheric asymmetry of equatorial ionization anomaly during solstices. *J. Geophys. Res.*: *Space Phys.*, *123*(12), 10283–10300. https://doi.org/10.1029/2018JA026055

Jiang, C. H., Yang, G. B., Liu, J., and Zhao, Z. Y. (2019a). A study of the *F*2 layer stratification on ionograms using a simple model of TIDs. *J. Geophys. Res.*: *Space Phys.*, *124*(2), 1317–1327. https://doi.org/10.1029/2018JA026040

Jiang, C. H., Hu, H., Yang, G. B., Liu, J., and Zhao, Z. Y. (2019b). A statistical study of the F2 layer stratification at the northern equatorial ionization anomaly. *Adv. Space Res.*, *63*(10), 3167–3176. https://doi.org/10.1016/j.asr.2019.01.038

Jimoh, O., Lei, J. H., Zhong, J. H., Owolabi, C., Luan, X. L., and Dou, X. (2019). Topside ionospheric conditions during the 7–8 September 2017 geomagnetic storm. *J. Geophys. Res.*: *Space Phys.*, *124*(11), 9381–9404. https://doi.org/10.1029/2019JA026590

Jin, Y. Y., Xing, Z. Y., Zhang, Q. H., Wang, Y., and Ma, Y. Z. (2019). Polar cap patches observed by the EISCAT Svalbard Radar: A statistical study of its dependence on the solar wind and IMF conditions. *J. Atmos. Solar-Terr. Phys.*, *192*, 104768. https://doi.org/10.1016/j.jastp.2018.01.011

Lan, J. P., Ning, B. Q., Li, G. Z., Zhu, Z. P., Hu, L. H., and Sun, W. J. (2018). Observation of short-period ionospheric disturbances using a portable digital ionosonde at Sanya. *Radio Sci.*, *53*(12), 1521–1532. https://doi.org/10.1029/2018RS006699

Lan, T., Zhang, Y. N., Jiang, C. H., Yang, G. B., and Zhao, Z. Y. (2018). Automatic identification of Spread F using decision trees. *J. Atmos. Solar-Terr. Phys.*, *179*, 389–395. https://doi.org/10.1016/j.jastp.2018.09.007

Lan, T., Jiang, C. H., Yang, G. B., Zhang, Y. N., Liu, J., and Zhao, Z. Y. (2019). Statistical analysis of low-latitude spread F observed over Puer, China, during 2015–2016. *Earth, Planets Space*, *71*, 138. https://doi.org/10.1186/s40623-019-1114-7

Le, H. J., Lou, L. B., Chen, Y. D., and Zhang, H. (2019). Anomaly distribution of ionospheric total electron content responses to some solar flares. *Earth Planet. Phys.*, *3*(6), 481–488. https://doi.org/10.26464/epp2019053

Lei, J. H., Dang, T., Wang, W. B., Burns, A., Zhang, B. Z., and Le, H. J. (2018b).

Long-lasting response of the global thermosphere and ionosphere to the 21 August 2017 solar eclipse. *J. Geophys. Res.*: *Space Phys.*, *123*(5), 4309–4316. https://doi.org/10.1029/2018JA025460

Lei, J. H., Huang, F. Q., Chen, X. T., Zhong, J. H., Ren, D. X., Wang, W. B., Yue, X. A., Luan, X. L., Jia, M. J., … Xue, X. H. (2018a). Was magnetic storm the only driver of the long-duration enhancements of daytime total electron content in the Asian-Australian sector between 7 and 12 September 2017?. *J. Geophys. Res.*: *Space Phys.*, *123*(4), 3217–3232. https://doi.org/10.1029/2017JA025166

Li, G. Z., Ning, B. Q., Abdu, M. A., Wang, C., Otsuka, Y., Wan, W. X., Lei, J. H., Nishioka, M., Tsugawa, T., … Yan, C. X. (2018a). Daytime F-region irregularity triggered by rocket-induced ionospheric hole over low latitude. *Prog. Earth Planet. Sci.*, *5*, 11. https://doi.org/10.1186/s40645-018-0172-y

Li, G. Z., Ning, B. Q., Li, A., Yang, S. P., Zhao, X. K., Zhao, B. Q., and Wan, W. X. (2018b). First results of optical meteor and meteor trail irregularity from simultaneous Sanya radar and video observations. *Earth Planet. Phys.*, *2*(1), 15–21. https://doi.org/10.26464/epp2018002

Li, G. Z., Ning, B. Q., Wang, C., Abdu, M. A., Otsuka, Y., Yamamoto, M., Wu, J., and Chen, J. S. (2018c). Storm-enhanced development of postsunset equatorial plasma bubbles around the meridian 120°E/60°W On 7–8 September 2017. *J. Geophys. Res.*: *Space Phys.*, *123*(9), 7985–7998. https://doi.org/10.1029/2018JA025871

Li, G. Z., Ning, B. Q., Zhao, X. K., Sun, W. J., Hu, L. H., Xie, H. Y., Liu, K. K., and Ajith, K. K. (2019). Low latitude ionospheric TEC oscillations associated with periodic changes in IMF Bz polarity. *Geophys. Res. Lett.*, *46*(16), 9379–9387. https://doi.org/10.1029/2019GL084428

Li, M., Yuan, Y. B., Wang, N. B., Liu, T., and Chen, Y. C. (2018). Estimation and analysis of the short-term variations of multi-GNSS receiver differential code biases using global ionosphere maps. *J. Geod.*, *92*(8), 889–903. https://doi.org/10.1007/s00190-017-1101-3

Li, N., Lei, J. H., Luan, X. L., Chen, J. S., Zhong, J. H., Wu, Q., Xu, Z. W., and Lin, L. K. (2019). Responses of the D region ionosphere to solar flares revealed by MF radar measurements. *J. Atmos. Solar-Terr. Phys.*, *182*, 211–216. https://doi.org/10.1016/j.jastp.2018.11.014

Li, Q. H., Hao, Y. Q., Zhang, D. H., and Xiao, Z. (2018). Nighttime enhancements in the midlatitude ionosphere and their relation to the plasmasphere. *J. Geophys. Res.*: *Space Phys.*, *123*(9), 7686–7696. https://doi.org/10.1029/2018JA025422

Li, Q. L., Liu, L. B., Balan, N., Huang, H., Zhang, R. L., Chen, Y. D., and Le, H. J. (2018). Longitudinal structure of the midlatitude ionosphere using COSMIC electron density profiles. *J. Geophys. Res.*: *Space Phys.*, *123*(10), 8766–8777. https://doi.org/10.1029/2017JA02492

Li, Q. L., Liu, L. B., Jiang, J. Z., Li, W. B., Huang, H., Yu, Y., Li, J. C., Zhang, R. L., Le, H. J., and Chen, Y. D. (2019). *α*-Chapman scale height: longitudinal variation and global modeling. *J. Geophys. Res.*: *Space Phys.*, *124*, 2083–2098. https://doi.org/10.1029/2018JA026286

Li, Z. X., Luan, X. L., and Ren, D. X. (2019). Longitudinal variations of the occurrence probability of the ionospheric F_1 layer peak at middle and high latitudes. *J. Geophys. Res.*: *Space Phys.*, *124*(11), 9592–9609. https://doi.org/10.1029/2018JA026236

Liu, G. Q., Huang, W. G., Shen, H., Aa, E., Li, M. X., Liu, S. Q., and Luo, B. X. (2019). Ionospheric response to the 2018 sudden stratospheric warming event at middle- and low-latitude stations over China sector. *Space Wea.*, *17*(8), 1230–1240. https://doi.org/10.1029/2019SW002160

Liu, H. T., Ding, F., Yue, X. A., Zhao, B. Q., Song, Q., Wan, W. X., Ning, B. Q., and Zhang, K. K. (2018). Depletion and traveling ionospheric disturbances generated by two launches of China's Long March 4B rocket. *J. Geophys. Res.*: *Space Phys.*, *123*(12), 10319–10330. https://doi.org/10.1029/2018JA026096

Liu, J., Zhang, D. H., Coster, A. J., Zhang, S. R., Ma, G. Y., Hao, Y. Q., and Xiao, Z. (2019a). A case study of the large-scale traveling ionospheric disturbances in the eastern Asian sector during the 2015 St. Patrick's Day geomagnetic storm. *Ann. Geophys.*, *37*(4), 673–687. https://doi.org/10.5194/angeo-37-673-2019

Liu, J., Zhang, D. H., Hao, Y. Q., and Xiao, Z. (2019b). The comparison of lunar tidal characteristics in the low-latitudinal ionosphere between East Asian and American sectors during stratospheric sudden warming events: 2009-2018. *J. Geophys. Res.*: *Space Phys.*, *124*(8), 7013–7033. https://doi.org/10.1029/2019JA026722

Liu, K. K., Li, G. Z., and Ning, B. Q. (2019). Possible evidence for small-scale wave seeding of equatorial plasma bubbles. *Adv. Space Res.*, *63*(11), 3612–3620. https://doi.org/10.1016/j.asr.2019.02.025

Liu, L. B., and Wan, W. X. (2018). Chinese ionospheric investigations in 2016–2017. *Earth Planet. Phys.*, *2*(2), 89–111. https://doi.org/10.26464/epp2018011

Liu, L. B., Le, H. J., Chen, Y. D., Zhang, R. L., Wan, W. X., and Zhang, S. R. (2019). New aspects of the ionospheric behavior over Millstone Hill during the 30-day incoherent scatter radar experiment in October 2002. *J. Geophys. Res.*: *Space Phys.*, *124*(7), 6288–6295. https://doi.org/10.1029/2019JA026806

Liu, M. R., Zhou, C., Wang, X., Ni, B. B., and Zhao, Z. Y. (2018). Numerical simulation of oblique ionospheric heating by powerful radio waves. *Ann. Geophys.*, *36*(3), 855–866. https://doi.org/10.5194/angeo-36-855-2018

Liu, Y., Lei, J. H., Yu, P. C., Liu, P. F., Ling, Y. M., Zhang, Z. K., and Cao, J. X. (2018a). Spontaneous emission of Alfvénic Branch oscillations from a strong inhomogeneous plasma flow. *Geophys. Res. Lett.*, *45*(1), 64–70. https://doi.org/10.1002/2017GL075611

Liu, Y., Lei, J. H., Yu, P. C., Ling, Y. M., Zhang, Z. K., Liu, P. F., and Cao, J. X. (2018b). Laboratory excitation of the Kelvin-Helmholtz instability in an ionospheric-like plasma. *Geophys. Res. Lett.*, *45*(9), 3846–3853. https://doi.org/10.1029/2018GL077550

Liu, Y., Zhou, C., Tang, Q., Li, Z. Q., Song, Y., Qing, H. Y., Ni, B. B., and Zhao, Z. Y. (2018c). The seasonal distribution of sporadic E layers observed from radio occultation measurements and its relation with wind shear measured by TIMED/TIDI. *Adv. Space Res.*, *62*(2), 426–439. https://doi.org/10.1016/j.asr.2018.04.026

Liu, Y., Zhou, C., Tang, Q., Chen, G. Y., and Zhao, Z. Y. (2019a). Geomagnetic conjugate observations of ionospheric disturbances in response to a North Korean underground nuclear explosion on 3 September 2017. *Ann. Geophys.*, *37*(3), 337–345. https://doi.org/10.5194/angeo-37-337-2019

Liu, Y., Zhou, C., Tang, Q., Kong, J., Gu, X. D., Ni, B. B., Yao, Y., and Zhao, Z. Y. (2019b). Evidence of mid- and low-latitude nighttime ionospheric *E*–*F* coupling: coordinated observations of sporadic *E* layers, *F* -region field-aligned irregularities, and medium-scale traveling ionospheric disturbances. *IEEE Trans. Geosci. Remote Sens.*, *57*(10), 7547–7557. https://doi.org/10.1109/TGRS.2019.2914059

Liu, Z. D., Fang, H. X., Weng, L. B., Wang, S. C., Niu, J., and Meng, X. (2019). A comparison of ionosonde measured f_oF_2 and IRI-2016 predictions over China. *Adv. Space Res.*, *63*(6), 1926–1936. https://doi.org/10.1016/j.asr.2019.01.017

Luo, W. H., Xiong, C., Zhu, Z. P., and Mei, X. F. (2018). Onset condition of plasma density enhancements: A case study for the effects of meridional wind during 17–18 August 2003. *J. Geophys. Res.*: *Space Phys.*, *123*(8), 6714–6726. https://doi.org/10.1029/2018JA025191

Lv, L. B., Li, Q. L., Hao, S. J., and Wu, Z. S. (2018). Study on scattering characteristic of AFAI in ionospheric heating by powerful high frequency waves. *Chinese J. Geophys.* (*in Chinese*), *61*(6), 2177–2185. https://doi.org/10.6038/cjg2018L0706

Ma, Y. Z., Zhang, Q. H., Xing, Z. Y., Jayachandran, P. T., Moen, J., Heelis, R. A., and Wang, Y. (2018a). Combined contribution of solar illumination, solar activity, and convection to ion upflow above the polar cap. *J. Geophys. Res.*: *Space Phys.*, *123*(5), 4317–4328. https://doi.org/10.1029/2017JA024974

Ma, Y. Z., Zhang, Q. H., Xing, Z. Y., Heelis, R. A., Oksavik, K., and Wang, Y. (2018b). The ion/electron temperature characteristics of polar cap classical and hot patches and their influence on ion upflow. *Geophys. Res. Lett.*, *45*(16), 8072–8080. https://doi.org/10.1029/2018GL079099

Meng, X., Fang, H. X., Li, G. Z., Weng, L. B., and Wang, S. C. (2019). Observations of evolution-type band-like structures of *F* region irregularities. *J. Geophys. Res.*: *Space Phys.*, *124*(2), 1426–1443. https://doi.org/10.1029/2018JA026091

Mo, X. H., and Zhang, D. H. (2018). Lunar tidal modulation of periodic meridional movement of equatorial ionization anomaly crest during sudden stratospheric warming. *J. Geophys. Res.*: *Space Phys.*, *123*(2), 1488–1499. https://doi.org/10.1002/2017JA024718

Mo, X. H., Zhang, D. H., Liu, J., Hao, Y. Q., Ye, J. F., Qin, J. S., Wei, W. X., and Xiao, Z. (2018). Morphological characteristics of equatorial ionization anomaly crest over Nanning region. *Radio Sci.*, *53*(1), 37–47. https://doi.org/10.1002/2017RS006386

Owolabi, C., Lei, J. H., Bolaji, O. S., Jimoh, O., Ruan, H. B., Li, N., Niu, X. J., and Yoshikawa, A. (2019). Investigation on the variability of the geomagnetic daily current during sudden stratospheric warmings. *J. Geophys. Res.*: *Space Phys.*, *124*(7), 6156–6172. https://doi.org/10.1029/2019JA026667

Priyadarshi, S., Zhang, Q. H., and Wang, Y. (2019). An empirical L-band scintillation model for a mid-latitude station, Weihai, China during the low solar activity period. *Sci. China*: *Technol. Sci.*, *62*(7), 1182–1190. https://doi.org/10.1007/s11431-017-9266-x

Ren, D. X., Lei, J. H., Wang, W. B., Burns, A., Luan, X. L., and Dou, X. K. (2019). A simulation study on the time delay of daytime thermospheric temperature response to the 27-day solar EUV flux variation. *J. Geophys. Res.*: *Space Phys.*, *124*(11), 9184–9193. https://doi.org/10.1029/2019JA027000

Ruan, H. B., Lei, J. H., Dou, X. K., Liu, S. Q., and Aa, E. C. (2018). An exospheric temperature model based on CHAMP observations and TIEGCM simulations. *Space Wea.*, *16*(2), 147–156. https://doi.org/10.1002/2017SW001759

Ruan, H. B., and Lei, J. H. (2019). Quantifying the impact of satellite sampling on the dynamic modeling of the upper thermosphere. *Space Wea.*, *17*(5), 757–766. https://doi.org/10.1029/2018SW002120

She, C. L., Yue, X. A., Hu, L. H., and Zhang, F. G. (2020). Estimation of ionospheric total electron content from a multi-GNSS station in China. *IEEE Trans. Geosci. Remote Sens.*, *58*(2), 852–860. https://doi.org/10.1109/TGRS.2019.2941049

Sui, Y., Fu, H. Y., Xu, F., Wang, R., and Jin, Y. Q. (2019). Estimation of Ionospheric Effects on Spacebore Twinsar-L SAR Interferograms. In *IGARSS 2019-2019 IEEE International Geoscience and Remote Sensing Symposium* (pp. 2081-2084). Yokohama: IEEE. DOI: 10.1109/IGARSS.2019.8899905

Sun, Y. Y., Liu, H. X., Miyoshi, Y., Liu, L. B., and Chang, L. C. (2018a). El Niño–Southern Oscillation effect on quasi-biennial oscillations of temperature diurnal tides in the mesosphere and lower thermosphere. *Earth*, *Planets Space*, *70*, 85. https://doi.org/10.1186/s40623-018-0832-6

Sun, Y. Y., Liu, J. Y., Lin, C. C. H., Lin, C. Y., Shen, M. H., Chen, C. H., Chen, C. H., and Chou, M. Y. (2018b). Ionospheric bow wave induced by the moon shadow ship over the continent of United States on 21 August 2017. *Geophys. Res. Lett.*, *45*(2), 538–544. https://doi.org/10.1002/2017GL075926

Sun, Y. Y. (2019). GNSS brings us back on the ground from ionosphere. *Geosci. Lett.*, *6*, 14. https://doi.org/10.1186/s40562-019-0144-0

Sun, Y. Y., Liu, H. X., Miyoshi, Y., Chang, L. C., and Liu, L. B. (2019a). El Niño–Southern Oscillation effect on ionospheric tidal/SPW amplitude in 2007–2015 FORMOSAT-3/COSMIC observations. *Earth*, *Planets Space*, *71*, 35. https://doi.org/10.1186/s40623-019-1009-7

Sun, Y. Y., Liu, J. Y., Wu, T. Y., and Chen, C. H. (2019b). Global distribution of persistence of total electron content anomaly. *Atmosphere*, *10*(6), 297. https://doi.org/10.3390/atmos10060297

Tian, Y. Y., Hao, Y. Q., Zhang, D. H., and Xiao, Z. (2019). Single crest phenomenon in the equatorial ionospheric anomaly region and its longitudinal distribution caused by nonmigrating tides. *Chinese J. Geophys.* (*in Chinese*), *62*(11), 4067–4081. https://doi.org/10.6038/cjg2019M0645

Wang, G. J., Shi, J. K., Bai, W. H., Galkin, I., Wang, Z., Sun, Y. Q. (2019). Global ionospheric scintillations revealed by GPS radio occultation data with FY3C satellite before midnight during the March 2015 storm. *Adv. Space Res.*, *63*(10), 3119–3130. https://doi.org/10.1016/j.asr.2019.01.028

Wang, H., Zhang, K. D., Zheng, Z. C., and Ridley, A. J. (2018). The effect of subauroral polarization streams on the mid-latitude thermospheric disturbance neutral winds: a universal time effect. *Ann. Geophys.*, *36*(2), 509–525. https://doi.org/10.5194/angeo-36-509-2018

Wang, H., Lühr, H., Zheng, Z. C., and Zhang, K. D. (2019). Dependence of the equatorial electrojet on auroral activity and in situ solar insulation. *J. Geophys. Res.*: *Space Phys.*, *124*(12), 10659–10673. https://doi.org/10.1029/2019JA027320

Wang, N., Guo, L. X., Zhao, Z. W., Ding, Z. H., and Lin, L. K. (2018). Spread-F occurrences and relationships with foF2 and h'F at low- and mid-latitudes in China. *Earth*, *Planets Space*, *70*, 59. https://doi.org/10.1186/s40623-018-0821-9

Wang, N., Guo, L. X., Ding, Z. H., Zhao, Z. W., Xu, Z. W., Xu, T., and Hu, Y. L. (2019a). Longitudinal differences in the statistical characteristics of ionospheric Spread-F occurrences at midlatitude in Eastern Asia. *Earth*, *Planets Space*, *71*, 47. https://doi.org/10.1186/s40623-019-1026-6

Wang, N., Guo, L. X., Zhao, Z. W., Ding, Z. H., Xu, T., and Sun, S. J. (2019b). A comparative study of ionospheric Spread-F and scintillation at low- and mid-latitudes in China during the 24th solar cycle. *Adv. Space Res.*, *63*(2), 986–998. https://doi.org/10.1016/j.asr.2018.10.010

Wang, S. C., Huang, S. X., and Fang, H. X. (2018). Dual-parameter regularization method in three-dimensional ionospheric reconstruction. *Ann. Geophys.*, *36*(5), 1255–1266. https://doi.org/10.5194/angeo-36-1255-2018

Wang, S. C., Huang, S. X., Lu, S., and Yan, B. (2019). 3-D ionospheric tomography using model function in the modified L-curve method. *IEEE Trans. Geosci. Remote Sens.*, *57*(6), 3135–3147. https://doi.org/10.1109/TGRS.2018.2881124

Wang, X., and Zhou, C. (2018). Electron density inversed by plasma lines induced by suprathermal electron in the ionospheric modification experiment. *Adv. Space Res.*, *61*(9), 2252–2258. https://doi.org/10.1016/j.asr.2018.02.001

Wang, X., Zhou, C., Liu, M. R., Honary, F., Ni, B. B., and Zhao, Z. Y. (2018a). Threshold of parametric instability in the ionospheric heating experiments. *Plasma Sci. Technol.*, *20*(11), 115301. https://doi.org/10.1088/2058-6272/aac71d

Wang, X., Zhou, C., Liu, M. R., Ni, B. B., and Zhao, Z. Y. (2018b). Density disturbance of small-scale field-aligned irregularities in the ionosphere heating experiments. *Plasma Sci. Technol.*, *20*(12), 125001. https://doi.org/10.1088/2058-6272/aadd45

Wang, X., Zhou, C., Xu, T., Honary, F., Rietveld, M., and Frolov, V. (2019). Stimulated electromagnetic emissions spectrum observed during an X-mode heating experiment at the European Incoherent Scatter Scientific Association. *Earth Planet. Phys.*, *3*(5), 391–399. https://doi.org/10.26464/epp2019042

Wang, Y., Zhang, Q. H., Jayachandran, P. T., Moen, J., Xing, Z. Y., Chadwick, R., Ma, Y. Z., Ruohoniemi, J. M., and Lester, M. (2018). Experimental evidence on the dependence of the standard GPS phase scintillation index on the ionospheric plasma drift around noon sector of the polar ionosphere. *J. Geophys. Res.*: *Space Phys.*, *123*(3), 2370–2378. https://doi.org/10.1002/2017JA024805

Wang, Z., Liu, H. X., Shi, J. K., Wang, G. J., and Wang, X. (2019). Plasma blobs concurrently observed with bubbles in the Asian-Oceanian sector during solar maximum. *J. Geophys. Res.*: *Space Phys.*, *124*(8), 7062–7071. https://doi.org/10.1029/2018JA026373

Weng, L. B., Lei, J. H., Doornbos, E., Fang, H. X., and Dou, X. K. (2018). Seasonal variations of thermospheric mass density at dawn/dusk from GOCE observations. *Ann. Geophys.*, *36*(2), 489–496. https://doi.org/10.5194/angeo-36-489-2018

Weng, L. B., Lei, J. H., Liu, H. X., Dou, X. K., and Fang, H. X. (2019). Thermospheric density cells at high latitudes as observed by GOCE satellite: Preliminary results. *Geophys. Res. Lett.*, *46*(21), 11615–11621. https://doi.org/10.1029/2019GL084951

Wu, J., Wu, J., Rietveld, M. T., Haggstrom, I., Xu, Z. W., and Zhao, H. S. (2018). The extending of observing altitudes of plasma and ion lines during ionospheric heating. *J. Geophys. Res.*: *Space Phys.*, *123*(1), 918–930. https://doi.org/10.1002/2017JA024809

Wu, J., Wu, J., Rietveld, M. T., Haggstrom, I., Xu, Z. W., Zhang, Y. B., Xu, T., and Zhao, H. S. (2019). The intensities of high frequency-enhanced plasma and ion lines during ionospheric heating. *J. Geophys. Res.*: *Space Phys.*, *124*(1), 603–615. https://doi.org/10.1029/2018JA025918

Wu, K., Xu, J. Y., Xiong, C., and Yuan, W. (2018). Edge plasma enhancements of equatorial plasma depletions observed by all-sky imager and the C/NOFS satellite. *J. Geophys. Res.*: *Space Phys.*, *123*(10), 8835–8849. https://doi.org/10.1029/2018JA025809

Wu, Y. W., Liu, R. Y., Zhang, B. C., Wang, W. B., Zhang, S. R., Zhang, Q. H., Hu, H. Q., and Lu, J. Y. (2019). The UT variation of the polar ionosphere based on

COSMIC observations. *J. Geophys. Res.*: *Space Phys.*, *124*(4), 3139–3148. https://doi.org/10.1029/2018JA026106

Xie, H. Y., Li, G. Z., Zhao, X. K., Hu, L. H., Wu, B. Y., and Ning, B. Q. (2018). Statistical study on the occurrences of postsunset ionospheric *E*, valley, and *F* region irregularities and their correlations over low-latitude Sanya. *J. Geophys. Res.*: *Space Phys.*, *123*(11), 9873–9880. https://doi.org/10.1029/2018JA025729

Xing, Z. Y., Zhang, Q. H., Han, D. S., Zhang, Y. L., Sato, N., Zhang, S. R., Hu, Z. J., Wang, Y., and Ma, Y. Z. (2018). Conjugate observations of the evolution of polar cap arcs in both hemispheres. *J. Geophys. Res.*: *Space Phys.*, *123*(3), 1794–1805. https://doi.org/10.1002/2017JA024272

Xu, L., Cheng, J., and Xu, J. S. (2019). Statistical features of TEC and ionospheric scintillation over the low latitude of China. *Adv. Space Res.*, *64*(10), 2164–2175. https://doi.org/10.1016/j.asr.2019.07.011

Xu, T., Rietveld, M., Wu, J., Ma, G. L., Hu, Y. L., Wu, J., and Li, Q. L. (2019). Polarization analysis of ELF/VLF waves generated by beating of two HF waves in the polar ionosphere. *J. Atmos. Solar-Terr. Phys.*, *195*, 105133. https://doi.org/10.1016/j.jastp.2019.105133

Yan, X. X., Sun, Y. Y., Yu, T., Liu, J. Y., Qi, Y. F., Xia, C. L., Zuo, X. M., and Yang, N. (2018). Stratosphere perturbed by the 2011 M_w9.0 Tohoku earthquake. *Geophys. Res. Lett.*, *45*(19), 10050–10056. https://doi.org/10.1029/2018GL079046

Yan, X. X., Yu, T., Sun, Y. Y., Xia, C. L., Zuo, X. M., Yang, N., Qi, Y. F., and Wang, J. (2020). Vertical structure of the ionospheric response following the M_w 7.9 Wenchuan earthquake on 12 May 2008. *Pure Appl. Geophys.*, *177*(1), 95–107. https://doi.org/10.1007/s00024-019-02175-7

Yang, G. B., Jiang, C. H., Lan, T., Huang, W. G., and Zhao, Z. Y. (2018). Ionosonde observations of daytime spread F at middle latitudes during a geomagnetic storm. *J. Atmos. Solar-Terr. Phys.*, *179*, 174–180. https://doi.org/10.1016/j.jastp.2018.07.009

Yang, J. T., Li, Q. L., Hao, S. J., Wang, J. G. (2018a). Theoretical analysis of parameter optimization for lower-ionosphere modulated excitation VLF/ELF waves. *Chinese J. Geophys.* (*in Chinese*), *61*(2), 477–483. https://doi.org/10.6038/cjg2018L0159

Yang, J. T., Li, Q. L., Wang, J. G., Hao, S. J., and Ma, G. L. (2018b). The polarization characteristics of ELF/VLF waves generated via HF heating experiments of the ionosphere by EISCAT. *Phys. Plasmas*, *25*(9), 092902. https://doi.org/10.1063/1.5044611

Yang, J. T., Wang, J. G., Li, Q. L., Wu, J., Che, H. Q., Ma, G. L., and Hao, S. J. (2019). Experimental comparisons between AM and BW modulation heating excitation of ELF/VLF waves at EISCAT. *Phys. Plasmas*, *26*(8), 082901. https://doi.org/10.1063/1.5095537

Yang, N., Le, H. J., Liu, L. B., and Zhang, R. L. (2018). Statistical behavior of the longitudinal variations of the evening topside mid-latitude trough position in both Northern and Southern Hemispheres. *J. Geophys. Res.*: *Space Phys.*, *123*(5), 3983–3997. https://doi.org/10.1029/2017JA025048

Yang, N., Yu, T., Le, H. J., Liu, L. B., Sun, Y. Y., Xia, C. L., Zuo, X. M., Yan, X. X., and Wang, J. (2019). The high-latitude trough in the Southern Hemisphere observed by Swarm — A satellite. *J. Geophys. Res.*: *Space Phys.*, *124*(11), 9475–9485. https://doi.org/10.1029/2019JA027169

Yang, S. G., Zhang, B. C., Liu, Y., Zhu, Y. G., Yang, X., Tian, C., Yue, F. L., Xu, P. K., and Jiang, J. M. (2019). Case studies: A possible mechanism for F2-lacuna formation. *Adv. Space Res.*, *64*(11), 2290–2304. https://doi.org/10.1016/j.asr.2019.08.036

Yu, T., Miyoshi, Y., Xia, C. L., Zuo, X. M., Yan, X. X., Yang, N., Sun, Y. Y., Yue, X. A., and Mao, T. (2018a). Solar dependence of equatorial *F* region irregularities observed by COSMIC radio occultations. *J. Geophys. Res.*: *Space Phys.*, *123*(11), 9775–9787. https://doi.org/10.1029/2018JA025936

Yu, T., Li, M. Y., Xia, C. L., Zuo, X. M., Liu, Z. Z., and Zhao, B. Q. (2018b). A new method for deriving equatorial plasma bubble velocity by tracing OI 630 nm all-sky images. *J. Geophys. Res.*: *Space Phys.*, *123*(11), 9619–9633. https://doi.org/10.1029/2018JA025332

Yu, T. T., Ren, Z. P., Yue, X. A., Yu, Y., and Wan, W. X. (2019). Comparison of thermospheric density between GUVI dayside limb data and CHAMP satellite observations: Based on empirical model. *J. Geophys. Res.*: *Space Phys.*, *124*(3), 2165–2177. https://doi.org/10.1029/2018JA026229

Yue, X. A., Hu, L. H., Wei, Y., Wan, W. X., and Ning, B. Q. (2018). Ionospheric trend over Wuhan during 1947–2017, Comparison between simulation and observation. *J. Geophys. Res.*: *Space Phys.*, *123*(2), 1396–1409. https://doi.org/10.1002/2017JA024675

Zhang, K. D., Wang, W. B., Wang, H., Dang, T., Liu, J., and Wu, Q. (2018). The longitudinal variations of upper thermospheric zonal winds observed by the CHAMP satellite at low and midlatitudes. *J. Geophys. Res.*: *Space Phys.*, *123*(11), 9625–9668. https://doi.org/10.1029/2018JA025463

Zhang, K. D., Liu, J., Wang, W. B., and Wang, H. (2019). The effects of IMF B_z periodic oscillations on thermospheric meridional winds. *J. Geophys. Res.*: *Space Phys.*, *124*(7), 5800–5815. https://doi.org/10.1029/2019JA026527

Zhang, M., Zhang, D. H., Hao, Y. Q., and Xiao, Z. (2019). A statistical study on L-band ionospheric amplitude scintillation in Shenzhen during 2011–2016. *Sci. Sin. Technol.* (*in Chinese*), *49*(12), 1570–1582. https://doi.org/10.1360/SST-2019-0093

Zhang, Q. H., Lockwood, M., Foster, J. C., Zong, Q. G., Dunlop, M. W., Zhang, S. R., Moen, J., and Zhang, B. C. (2018). Observations of the step-like accelerating processes of cold ions in the reconnection layer at the dayside magnetopause. *Sci. Bull.*, *63*(1), 31–37. https://doi.org/10.1016/j.scib.2018.01.003

Zhang, R. L., Liu, L. B., Balan, N., Le, H. J., Chen, Y. D., and Zhao, B. Q. (2018). Equatorial ionospheric disturbance field-aligned plasma drifts observed by C/NOFS. *J. Geophys. Res.*: *Space Phys.*, *123*(5), 4192–4201. https://doi.org/10.1029/2018JA025273

Zhang, R. L., Liu, L. B., Le, H. J., and Chen, Y. D. (2019). Equatorial ionospheric electrodynamics over Jicamarca during the 6–11 September 2017 space weather event. *J. Geophys. Res.*: *Space Phys.*, *124*(2), 1292–1306. https://doi.org/10.1029/2018JA026295

Zhao, B. Q., Yang, C. J., Cai, Y. H., Jin, Y. Y., Yu, L., Ding, F., Yue, X. N., and Wan, W. X. (2019). East–west difference in the ionospheric response of the March 1989 great magnetic storm throughout East Asian region. *J. Geophys. Res.*: *Space Phys.*, *124*(11), 9364–9380. https://doi.org/10.1029/2019JA027108

Zhao, C. H., Yuan, Y. B., Zhang, B. C., and Li, M. (2019). Ionosphere sensing with a low-cost, single-frequency, multi-GNSS receiver. *IEEE Trans. Geosci. Remote Sens.*, *57*(2), 881–892. https://doi.org/10.1109/TGRS.2018.2862623

Zhao, J. Q., and Zhou, C. (2018). On the optimal height of ionospheric shell for single-site TEC estimation. *GPS Solut.*, *22*(2), 48. https://doi.org/10.1007/s10291-018-0715-0

Zhao, J. Q., and Zhou, C. (2019). Validation and application of optimal ionospheric shell height model for single-site estimation of total electron content. *Ann. Geophys.*, *37*(2), 263–271. https://doi.org/10.5194/angeo-37-263-2019

Zhao, X. R., Sheng, Z., Li, J. W., Yu, H., and Wei, K. J. (2019). Determination of the "wave turbopause" using a numerical differentiation method. *J. Geophys. Res.*: *Atmos.*, *124*(20), 10592–10607. https://doi.org/10.1029/2019JD030754

Zhong, J. H., Lei, J. H., Yue, X. A., Luan, X. L., and Dou, X. K. (2019a). Middle-latitudinal band structure observed in the nighttime ionosphere. *J. Geophys. Res.*: *Space Phys.*, *124*(7), 5857–5873. https://doi.org/10.1029/2018JA026059

Zhong, J. H., Lei, J. H., Yue, X. A., Wang, W. B., Burns, A. G., Luan, X. L., and Dou, X. K. (2019b). Empirical orthogonal function analysis and modeling of the topside ionospheric and plasmaspheric TECs. *J. Geophys. Res.*: *Space Phys.*, *124*(5), 3681–3698. https://doi.org/10.1029/2019JA026691

Zhou, C., Liu, Y., Tang, Q., Gu, X. D., Ni, B. B., and Zhao, Z. Y. (2018a). Investigation on the occurrence of mid-latitude E-region irregularity by Wuhan VHF radar and its relationship with sporadic E layer. *IEEE Trans. Geosci. Remote Sens.*, *56*(12), 7207–7216. https://doi.org/10.1109/TGRS.2018.2849359

Zhou, C., Tang, Q., Huang, F. Q., Liu, Y., Gu, X. D., Lei, J. H., Ni, B. B., and Zhao, Z. Y. (2018b). The simultaneous observations of nighttime ionospheric *E* region irregularities and *F* region medium-scale traveling ionospheric disturbances in midlatitude China. *J. Geophys. Res.*: *Space Phys.*, *123*(6), 5195–5209. https://doi.org/10.1029/2018JA025352